NIST Technical Note 2201

Laser-assisted atom probe tomography of c-plane and m-plane InGaN test structures

Norman A. Sanford
Paul T. Blanchard
Matthew D. Brubaker
Ashwin K. Rishinaramangalam
Qihua Zhang
Alexana Roshko
Daniel F. Feezell
Benjamin D. B. Klein
Albert V. Davydov

This publication is available free of charge from:
https://doi.org/10.6028/NIST.TN.2201

National Institute of
Standards and Technology
U.S. Department of Commerce

NIST Technical Note 2201

Laser-assisted atom probe tomography of c-plane and m-plane InGaN test structures

Norman A. Sanford
Paul T. Blanchard
Matthew D. Brubaker
Applied Physics Division
Physical Measurement Laboratory

Ashwin K. Rishinaramangalam
Electrical and Computer Engineering Department
University of New Mexico,
Albuquerque, NM

Qihua Zhang
Department of Electrical and Computer Engineering
Georgia Institute of Technology,
Atlanta, GA

Alexana Roshko
Applied Physics Division
Physical Measurement Laboratory

Daniel F. Feezell
Electrical and Computer Engineering Department
University of New Mexico,
Albuquerque, NM

Benjamin D. B. Klein
Department of Electrical and Computer Engineering
Georgia Institute of Technology,
Atlanta, GA

Albert V. Davydov
Materials Science and Engineering Division
Material Measurement Laboratory

This publication is available free of charge from:
https://doi.org/10.6028/NIST.TN.2201

April 2022

U.S. Department of Commerce
Gina M. Raimondo, Secretary

National Institute of Standards and Technology
Laurie E. Locascio, NIST Director and Undersecretary of Commerce for Standards and Technology

National Institute of Standards and Technology Technical Note 2201
Natl. Inst. Stand. Technol. Tech. Note 2201, 51 pages (April 2022)
CODEN: NTNOEF

Abstract

Laser-assisted atom probe tomography (APT) was used to measure the indium concentrations of *c*-plane GaN/$In_xGa_{1-x}N$/GaN samples and the results were compared with Rutherford backscattering analysis (RBS). Four sample types were examined with x = 0.030, 0.034, 0.056, and 0.112. The estimated RBS uncertainty for In was ± 0.5 at.%. These samples were grown by metalorganic vapor-phase epitaxy (MOCVD) and their respective thicknesses were 330 nm, 327 nm, 360 nm, and 55 nm. APT data were collected at laser pulse energies (PEs) selectable within (2—1000) fJ; base temperatures were variously 54 K, and 26 K. For the x values indicated, APT returned In concentrations within RBS uncertainty for PEs of (2—50) fJ, (2—10) fJ, (2—100) fJ, and (2—50) fJ. Assigning the (14—16) Da range to complexes of NH_x or N_2H_x did not significantly change the measurements of In concentrations, nor did parsing the data into single-hit or multiple-hit detector events. In concentrations were comparable for regions-of-interest (ROIs) which encompassed the InGaN portions or were confined to 20 nm diameter, coaxial ROIs. Stoichiometry was found in the GaN portions if the PE was ~ 10 fJ and analyses confined to 20 nm-diameter, coaxial ROIs. *m*-plane oriented tips were derived from *c*-axis, MOCVD-grown, core-shell, GaN/$In_xGa_{1-x}N$ nanorod heterostructures. Compositional analysis along [0001] (transverse to the long axis of the tip), of these *m*-plane samples revealed a spatial asymmetry in the Ga^{2+}/Ga^{1+} charge-state ratio (CSR) and a corresponding asymmetry in the resultant tip shape along this direction; no asymmetry in CSR or tip shape was observed for analysis along $[\bar{1}2\bar{1}0]$. Simulations revealed that the surface electric field at the tip apex is dominated by the presence of a conducting *p*-type inversion layer, which develops under typical sample-electrode bias conditions for the *n*-type doping levels considered.

Key words

atom probe tomography; charge state ratio; field evaporation; GaN; III-nitride compound semiconductors.

Table of Contents

List of Tables

List of Figures

1. Introduction

Laser-assisted atom probe tomography (APT) is gaining wide acceptance for 3-dimensional (3D), sub-nm-resolved, chemical mapping of metals, semiconductors, nanowires, superconductors, oxides, and biological materials.[1-4] In this paper we are only concerned with laser-assisted atom probe and not voltage-pulsed methods. Therefore, we adopt the abbreviation "APT" rather than "L-APT" –which is sometimes used to distinguish the laser-assisted approach from voltage pulsing. Very briefly, APT may be summarized as follows: a nano-needle shaped specimen is maintained at a base temperature $T \approx 50$ K under ultra-high vacuum and biased at a voltage that is held just below the threshold for field evaporation of ions. The corresponding electric field strength (on the vacuum side of the vacuum/tip interface) to establish this condition is on the order of 10 V/nm. Field evaporation is then triggered by a pulsed laser incident upon the specimen. The mechanism is generally assumed to arise from a thermally-driven pathway whereby transient temperature increases induced by the laser momentarily reduce the threshold for field evaporation at the specimen apex and ions are then emitted synchronously with the laser pulse frequency. One should not confuse APT with laser ablation; APT generally employs incident laser pulse energies that are many orders of magnitude below the threshold for ablation. Ions field-evaporated from the specimen and accelerated in the applied electric field are picked up by a two-dimensional detector, which enables recording their impact locations and times-of-flight. The accumulated data are used to calculate a 3D compositional map, or "reconstruction," of the specimen by computing the original location of each elemental specie with the corresponding ion identified by its time-of-flight. The maximum analysis depth corresponds to the reduction in length of the needle-shaped specimen due to ions lost by field evaporation. In principle, the process may proceed indefinitely but practical considerations often limit the collection of between 10^5 to 10^8 ions. To put this into context: for reconstruction 10 listed in Table 3, a total of 4.8×10^6 ions were recorded, which corresponded to an analysis depth of ~ 100 nm. In our prior work, a GaN nanowire was run to an analysis depth of ~ 1.6 μm where 3.12×10^8 ions were recorded.[5]

Closer to the topic at hand, Rigutti, et al.[6] have surveyed APT analysis of wide-bandgap, III-N compound semiconductor device structures, which includes LEDs, lasers, and high electron-mobility transistors. As they succinctly noted, "*Due to the relatively high rate of success for the analysis and to the straightforward interpretation of their mass spectra, III-N materials have become a model system for the study of compositional biases in APT, which may occur in a much broader class of compounds.*" Studies of APT compositional biases in other wide-bandgap materials, including ZnO and MgO, have also been reported.[7] Here, "compositional bias," is the departure of an APT-derived, spatially-resolved elemental map from a specimen's true, physical make up. Composition biases are manifestations of the practical inability of APT to correctly count and identify all the atoms that are field evaporated from a specimen. Such biases may emerge via numerous factors including ambiguous identification of mass-spectral peaks, inability to reliably deconvolve overlapping peaks, multiple ions simultaneously detected, and the emission of neutral species. The latter mechanism is believed to occur directly, or by processes involving the dissociation of field-evaporated molecular complexes. These issues have been discussed at length.[1, 3, 6, 8]

Composition bias effects that arise in studies of III-N materials can strongly depend upon instrumental factors such as specimen-electrode voltage (SV), incident laser pulse energy (PE), laser pulse repetition rate (f), and the laser wavelength (λ) used. Electrostatically induced specimen fracture can often be mitigated by exploiting the interplay between PE and SV such that elevated PE will allow reducing SV, and thus reduce the likelihood of fracture, while maintaining the desired detection rate (DR) of ions. However, elevated PE applied to GaN specimens will often return a compositional bias that indicates an (unphysical) deficiency of nitrogen. [6, 7, 9] The reverse can also occur ─ a reduced PE and elevated SV can return a composition that is biased rich in N. Such compositional biases are unphysical in GaN because the material exists as a line compound and will thus decompose if its true stoichiometry deviates even slightly from 50% Ga and 50% N.[10] Consequently, situations involving, say, APT analysis of a particularly fragile GaN heterostructure specimen may force an operator to choose data acquisition conditions where the SV is relatively low and it is known beforehand that the returned concentrations of Ga and N will be incorrect—which may immediately call into question the analytical accuracy of APT for determining the concentration and distribution of various other alloy constituents and dopants that may be present in the specimen.

In recent years, APT applied to the study of III-nitrides and other wide-bandgap materials has evolved from employing a laser operating in the visible ($\lambda = 532$ nm, Ref.[11]) and now more typically uses near-ultraviolet lasers, e.g., $\lambda = 343$ nm or 355 nm.[7, 9] Evidence also suggests that operating at even shorter wavelength, notably $\lambda = 258$ nm, should yield improved mass resolution and signal-to-noise ratio in APT studies of metals, semiconductors and insulators.[12] Additionally, it was recently reported that a reduction in the relative evaporation field differences between Si and SiO_2 interfaces was observed for APT operation with $\lambda = 266$ nm compared to $\lambda = 355$ nm. [13] Nonetheless, there does not yet seem to be a conclusively superior laser wavelength for APT.

Controversy also exists as to the nature of the underlying pathways, thermal or otherwise, responsible for laser-assisted field evaporation. For example, an APT study ($\lambda = 355$ nm) of MgO ascribed the photogeneration of holes and the role of surface states as primary mechanisms for field evaporation since λ was well below the bulk bandgap (≈ 7.7 eV) for MgO.[14] For GaN with $\lambda = 355$ nm, Diercks et al.[15] argue for the possibility of an athermal field evaporation mechanism even though 355 nm corresponds closely to the low-temperature absorption edge of bulk GaN (≈ 3.48 eV) [16, 17], which suggests that a thermal pathway cannot be excluded. An instrumentation concept enabling a photoionization pathway for APT has been proposed; this approach would replace the conventional, near-UV laser with an extreme-UV (EUV) laser.[18, 19] A prototype EUV-equipped APT tool with $\lambda = 29.6$ nm (≈ 42 eV) was indeed constructed and initial results on SiO_2 (amorphous fused silica) showed recovery of the correct stoichiometry.[20] Moreover, the EUV-equipped APT tool has also shown promise on a variety of III-nitride semiconductor samples. [21] Finally, besides correlations with the λ and PE used, compositional biases may also be influenced by the presence of defects in the specimen, and the crystallographic direction along which the analyses were performed.[6, 22, 23]

Clearly, APT presents numerous unresolved issues associated with the mechanisms responsible for field evaporation, composition biases, and their interrelation. However, perhaps the main question confronting a materials engineer supporting III-nitride development boils down to: "If I operate my atom probe tool in a fashion that assures analysis to the required depth without fracturing the specimen, what can I expect in terms of spatially-resolved analytical sensitivity, precision, and uncertainty for measurements of the dopants and alloy constituents of interest?" This paper is primarily addressed to workers posing that question.

In our study of GaN/$In_xGa_{1-x}N$/GaN multilayer samples we have compiled APT data that were collected under various operational conditions. For *c*-plane, (0001), specimens taken from samples of planar epitaxial films, the values of x derived from APT are compared to results obtained from Rutherford backscattering analysis (RBS) performed on the same samples. For *m*-plane, $(10\bar{1}0)$, quantum well (QW) specimens taken from core-shell micropost samples, the APT-derived results for x are compared with values of x that have been previously calibrated by photoluminescence studies at the University of New Mexico. Variously, for both *c*-plane and *m*-plane samples, the (APT) reconstructed layer thicknesses are calibrated by means of separate X-ray diffraction (XRD) and transmission electron microscopy (TEM) measurements. A key contribution of this paper for the *c*-plane samples is to obtain APT tool operational conditions that return indium concentrations that conform, within experimental error, to RBS. We then apply the RBS-anchored tool conditions to APT analysis of the *m*-plane samples and find that the indium concentration in the QWs conforms to what is expected from photoluminescence.

Interestingly, we observed an asymmetric, spatially-varying artifact in GaN charge state ratios (CSRs) for the *m*-plane GaN specimens when the analysis direction is along [0001], i.e., transverse to the long axis of the specimen tip. The effect is absent when the analysis is performed in the non-polar $[\bar{1}2\bar{1}0]$ direction; it is also absent when analysis is performed in non-polar directions on *c*-plane tips. As will be discussed at length in Section 3.1.2, the feature is attributed to an observed asymmetric evolution of the apex of an *m*-plane tip such that the apex displaces toward the -*c* direction as ions are field evaporated away. By contrast, *c*-plane tips generally evolve symmetrically during APT.

In our terminology, "specimen(s)" or "tip(s)", and "lamella(e)" are prepared from "samples" for examination by APT and TEM, respectively. A focused ion beam (FIB) tool, which incorporates a field-emission scanning electron microscope (FESEM), was used to prepare all tips and lamellae. Finally, we make interchangeable use of the terms "measured composition" and "composition" in referring to APT results—and emphasize that such output will often differ from the true, *physical composition* of the specimen at hand.

Following this introduction, the paper is organized as follows: Section 2 describes the samples used in this study and specimen preparation therefrom. Section 3 presents the results of APT performed on a series of specimens taken from *c*-plane GaN/$In_xGa_{1-x}N$/GaN multilayer samples. Analysis of specimens prepared from an *m*-plane, QW sample is also presented. A brief summary of the electrostatic analysis is presented in Section 4 with a more extensive development presented in Ref. [24]. A discussion of experimental and analytical uncertainties is included in Section 5 and conclusions are presented in Section 6.

2. Samples Examined

2.1. c-plane GaN/InxGa1-xN/GaN multilayers

This collection of samples consists of 4 separate metalorganic chemical vapor deposition (MOCVD) growth runs with respective RBS-determined values of *x* of: 0.112, 0.056, 0.034, and 0.030; the corresponding layer thicknesses, as variously determined by XRD or growth rate, are given in Table 1. For all cases, the estimated uncertainty in RBS measurements of In is ± 0.5 at.%. These samples were used in an entirely separate study discussed in Ref. [25] and preliminary RBS results were given therein; the RBS analysis presented in this paper was separately performed, but the results are quite similar to that earlier work. APT specimen tips were prepared using FIB techniques that have been discussed at length elsewhere.[26, 27] FIB techniques for preparing TEM lamellae are well established and generally documented in FIB operation manuals.

Table 1. Summary of c-plane InxGa1-xN test structures by sample type.

sample type	In concentration (RBS)		layer thickness (nm)		
	at.%	*x*	*L*	L_c	Measurement method
h	5.60	0.112	55.4	13.2	XRD
f	2.8	0.056	360	23.0	
d	1.7	0.034	327	20.0	
c	1.5	0.030	330	20.0	Estimated from growth rate

The RBS-determined indium concentration is reported in at.%, with an estimated uncertainty of ± 0.5 at.%. Indium concentrations expressed in at.% are multiplied by 0.02 to convert to mole fraction *x*. The thicknesses of the $In_xGa_{1-x}N$ layer and capping layer are labeled *L* and L_c, respectively.

2.2. *m*-plane GaN/$In_xGa_{1-x}N$/GaN QW structures

These samples were arrays of *c*-axis oriented, MOCVD-grown, core-shell microposts with QWs grown on the *m*-plane sidewall facets; fabrication details are described elsewhere.[28-30] The micropost core was comprised of lightly-doped (free carrier concentration in the mid-low $10^{17}cm^{-3}$), *n*-type GaN grown using pulsed-MOCVD to achieve a high vertical growth rate and minimal lateral growth. The growth was performed under a H_2/N_2 mixed atmosphere at 13.3 kPa and 940°C. The V/III ratio employed during the growth was ~100. The growth of the core section was followed by the growth of three pairs of InGaN/ GaN quantum-well shells around the posts in an N_2 atmosphere using a high V/III ratio (~10,000). Figure 1 (a) illustrates an array of these structures and Fig. 1 (b) shows a TEM image that illustrates thicknesses of the GaN capping layer, $In_xGa_{1-x}N$ QWs, and GaN barrier layers. Both the APT specimens and TEM lamellae were fabricated using FIB techniques that were very similar to those used for the *c*-plane samples.

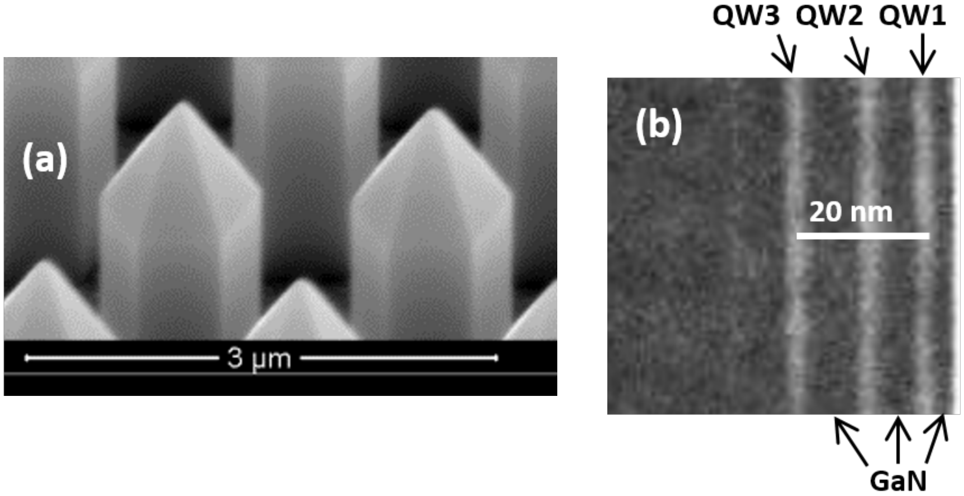

Figure 1

(a) FESEM image of GaN/InGaN core-shell microposts. The vertical sidewalls conform to the $\{10\bar{1}0\}$ family of *m*-planes. The Ga-polar apex points in the [0001] direction (+*c*). (b) TEM cross section of the core-shell quantum wells (QWs). The QWs reside on *m*-planes and QW1 is nearest the surface. The GaN capping layer is indicated to the extreme right and the two GaN barrier layers reside between the QWs.

3. APT analysis of samples

3.1. Overview

APT data were acquired with a LEAP 4000XSi atom probe tool manufactured by CAMECA Instruments; data analysis was performed using the IVAS software package (primarily version 3.6.14 with confirming analyses performed using version 3.8.2) provided by the same company. For all cases considered in this paper, the specimen-detector flight length was 90 mm. The laser installed on the tool operates at $\lambda = 355$ nm with a pulse width of ≈ 8 ps and is focused to a diameter of ≈ 2 µm at the specimen tip. In our usage, “voltage,” “specimen voltage,” SV, and “bias voltage” all refer to the electrode-tip voltage bias that produces field evaporation of ions from the specimen. In this context, “field evaporation,” is defined by Miller.[31] Additionally, common IVAS data analysis outputs and parameters are abbreviated as: reconstruction (recon), region of interest (ROI), top-level ROI (TLROI), detector efficiency (DE), image compression factor (ICF), and sphere-cone-radius-ratio (S/C). For all recon cases presented, we used the “Tip Profile” method in the IVAS software whereby an FESEM image of the as-FIB-prepared specimen is imported into the software. Additionally, an FESEM image of the tip shape after data acquisition was used to estimate S/C for inclusion in the IVAS analysis. For all data acquisition cases presented in this paper, f = 250 kHz.

Mass-spectral peak assignments are given in Table 2. As will be discussed in the following sections, the detected quantities of these species depend upon tool operational conditions and the selection and placement of ROIs within a TLROI. Following Mancini, et al., we typically adopt the convention that the peak at 14 Da is assigned to the N_2^{2+} ion.[7] Of course, exclusively assigning 14 Da to N_2^{2+} is not necessarily valid since an admixture or predominance of N^{1+} may certainly exist, but there is insufficient information to reliably deconvolve the possible separate contributions of the two ions. On the other extreme, Di Russo, et al. argue that the 14 Da assignment should be associated with N^{1+}.[8] However, there is no a priori reason to assume that exclusively assigning 14 Da to N^{1+} or N_2^{2+} should generalize to the $In_xGa_{1-x}N$ ternary alloy over a span of x within technological interest and over a range of APT tool conditions that prioritize specimen longevity. As we will illustrate by example cases, the effect of interchanging the 14 Da assignment between N^{1+} and N_2^{2+} serves mostly to displace the PE that will return a physically realistic N concentration toward 50 at.%. However, we rarely observe cases of tool conditions that will simultaneously yield an indium concentration in conformance with RBS results with a N concentration of ≈ 50 at.%. Therefore, for the purposes of this paper, it is immaterial to argue for the validity of which N molecular specie to assign to 14 Da and far more useful to the APT practitioner to report the consequence of the choice.

Over the range of x considered in this paper, the volume of the $In_xGa_{1-x}N$ primitive cell does not substantially deviate from that of GaN—with regards to its influence on computing reconstructions. In particular, the volume contributed per ion for GaN is 0.0114 nm^3 as deduced from tabulated XRD data.[32] The highest RBS-determined indium concentration we consider in this paper is x = 0.112 (sample h). Our XRD analysis, in conjunction with the results of Ref. [33], allow us to estimate the volume occupied per ion is 0.0117 nm^3 for the case of $x = 0.112$. Therefore, for simplicity, we assign the volumetric contribution per ion to 0.0114 nm^3 for all samples considered since correcting for the crystallographic cell volume of even our highest indium-containing sample will have a negligible effect on the reconstructions.

Finally, we distinguish between two reconstruction conventions available in the IVAS software; these we designate as “specimen view” and “detector view.” The specimen view scheme is preferred if one desires a reconstruction that properly conforms to the 3-dimensional spatial orientation of the physical specimen. On the other hand, if one doesn’t require a recon to have full spatial conformity with the original specimen tip then the detector view will suffice. The distinction between these reconstruction schemes is illustrated in Fig. 5(a). And discussed further below.

Table 2. Typical ranged species, associated charge states observed, and comments related to reconstructions.

	charge state			volume contributed to recon per ranged specie (nm^3)	comments
	1^+	2^+	3^+		correcting the per-atom volume contribution in a recon for the true InGaN alloy composition is insignificant.
specie	ranged peaks (Da)				
Ga	68.926, 70.925	34.463, 35.462	22.975, 23.642	0.0114	
N	14.003	7.0015	NA		
In	112.90, 114.90	56.450, 57.450	37.630		
N_2	28.006	14.003, 14.5	NA	0.0228	
NH	ranged as N	ranged as N		0.0114	H contributes no volume to recon
N_2H_2	ranged as N_2	ranged as N_2		0.0228	
N_2H_4					
N_3	42.009			0.0342	NA
GaN	NA	41.464, 42.464		0.0228	
GaN_2		48.466, 49.465		0.0342	prominent when PE > 1 pJ.
GaN_3		55.467, 56.467		0.0456	
H	various H species routinely seen	NA		NA	not ranged
H_2					
H_3					

3.1.1. c-plane, GaN/In$_x$Ga$_{1-x}$N/GaN multilayer samples

The (≈ 55 nm) thickness of the InGaN layer in sample h provides a convenient marker for constraining the selection of recon parameters. Such constraints then help provide justification for selecting recon parameters used for analyses of the other multilayer specimens (samples f, d, and c) that have thicker InGaN regions but were not run long enough in APT to penetrate both top and bottom InGaN/GaN interfaces. Indeed, the InGaN layers are inconveniently thick for these samples (see Table 1) and excessive APT operational time would be required to penetrate both top and bottom interfaces. For specimens from samples f, d, and c, comparative FESEM imaging before and after APT were used to set geometric constraints in the reconstructions.

Tables 3—6 give detailed enumeration of all the recon cases for c-plane samples h, f, d, and c. The column headings for N, Ga, and In refer to the integrated concentrations (at. %) within the ROIs for the respective species. In all cases, the IVAS-computed concentration, with background subtracted, of a specie included both elemental assignments and contributions that were software-decomposed from complex molecular ions. For specimen temperatures of 54 K and 26 K, results are shown for several PE cases ranging over (2—1000) fJ and (2—50) fJ, respectively. Additionally, the IVAS fitting parameters used for each recon are also given in the table.

The (x, y, z) coordinate system for recons follows the IVAS convention, and the z axis is nominally collinear to the crystallographic *c* axis of a specimen tip. However, it should be borne in mind that in IVAS detector view, the +z direction points from the recon apex to its base. For specimen view of the same reconstruction, the +z direction points from the base to the apex; the *x* and *y* axes are the same in both views. These distinctions are illustrated in Fig. 5 (a). Our *c*-plane samples are grown with Ga-polarity. Thus, the crystallographic +*c* direction, i.e. [0001], for a specimen tip is antiparallel to the IVAS z-axis for a recon presented in detector view but conforms with the direction of the IVAS z-axis if the recon is cast into specimen view.

The recon cases in Tables 3—6 compare IVAS-computed compositions for TLROIs with compositions computed within cylindrical ROIs, which are 20 nm in diameter and coaxial with the TLROI. The choice and orientation of such a cylindrical ROI is motivated by APT results for GaN whereby IVAS will typically return approximate stoichiometry when the analysis is constrained to such an ROI for cases where the PE is roughly 10 fJ, and the other operational parameters, i.e., f, T, DR are 250 kHz, 54 K, and 0.4 %, respectively; an example of this trend is evident in Fig. 11 (b). Tables 3—6 also present comparative results of IVAS-derived composition for cases of 14 Da assigned to N^{1+} (rather than N_2^{2+}), with either single or multiple detector events used in the analysis. The volumetric differences in the computed ROIs for these two cases of 14 Da assignments are reflected in the values of L_R indicated, but these geometrical effects are minor and do not change our overall conclusions.

Table 3. Data acquisition and analysis parameters per reconstruction (recon) for specimens from sample h.

recon		ROI 1				ROI 2			DR	DE	ICF	L_R	S/C	ID
	T	PE	N	Ga	In	N	Ga	In						
1(a)	54	2	58	37	5.2	58	37	5.2	0.4	0.19	2.0	52	1.12	1-6_01256v21
1(b)			58	37	5.0	NA						NA		…v23
1(c)			55	40	5.3	55	40	5.8				50		…v24
1(d)			55	40	5.3	NA						NA		…v25
2		5	57	38	5.0	56	39	5.1		0.32		52	1.00	2-1_01257v10
3(a)		10	55	40	5.3	55	40	5.4		0.32		54	1.02	2-2_01258v09
3(b)			55	40	5.2	NA						NA		…v11
3(c)			53	42	5.6	52	42	5.9				50		…v12
3(d)			53	41	5.6	NA						NA		…v13
4		50	48	46	6.0	51	43	5.8		0.26		52	1.20	2-3_01259v06
5		100	43	51	6.0	48	46	5.9		0.28			1.14	6-2_01020v07
6		1000	16	76	8.4	19	72	9.1		0.24			1.20	5-2_01030v06
7	26	2	58	37	4.8	57	38	5.1	0.4	0.29	2.0	52	1.10	1-2_01252v18
8		5	56	39	4.9	55	40	5.1		0.27			1.13	1-3_01253v12
9		10	55	40	5.4	55	40	5.8		0.29			1.12	1-4_01254v05
10		50	48	46	5.8	52	42	6.2		0.23			1.00	1-5_01255v09

The column heading enumerating individual reconstructions is abbreviated "recon." ROI 1 is a cylindrical region that encloses all of the InGaN portion of the TLROI but excludes the top and bottom GaN layers. ROI 2 is a 20-nm-diameter cylindrical subset of ROI 1 that is placed coaxial with the TLROI. Note that L_R (nm) is the length of both ROIs and is set ≈ 3 nm less than the XRD-determined InGaN layer thickness in order to accommodate irregularities and tilts of the GaN/InGaN interfaces. N, Ga, and In are column headings for the respective elemental concentrations (at.%) within each ROI. ID lists verbose identifications of each reconstruction to assist in future reference (e.g. for recon 1, "1-6" is the specimen tip number, "01256" is the datafile number, "v21" is the version of the recon). Other abbreviations are given in the text. Recons 1 and 3 are further subdivided into a—d cases where 14 Da is assigned to N^{1+} or N^{2+} and single-hit or multi-hit detection events are separately considered for either choice of ionized N specie. In recons 1(a—d) and 3(a—d), (a) denotes 14 Da assigned to N_2^{2+} and all detection events used; (b) denotes 14 Da assigned to N_2^{2+} and only single detection events used; (c) denotes 14 Da assigned to N^{1+} and all detection events used; (d) denotes 14 Da assigned to N^{1+} and only single detection events used The all-detection-events cases for alternatively assigning 14 Da to either N_2^{2+} or N^{1+} use the same IVAS fitting parameters, which is valid since they return, within estimated uncertainties for S/C and interface flatness, equivalent results for L_R in both cases. However, for the single-detection-event cases there are necessarily fewer ions counted for analysis since the multiple-detection events are discarded. Therefore, for those cases we size ROI 1 to encompass the apparent thickness of the InGaN layer and no attempt is made to scale its length to conform to the actual, physical layer thickness. Moreover, we omit analyses in ROI 2 since such scaling issues prevent setting its diameter for meaningful comparison with all-detection-event cases. Subdivision of recons 1 and 3 into these a—d cases are included to illustrate the trend that insofar as one seeks correlation of APT and RBS results within the uncertainty of the latter, it makes little difference if one simply chooses to count all detector hits and assign 14 Da to N_2^{2+}. In all other recons appearing in the table, 14 Da is assigned to N_2^{2+} and all detection events are used.

Table 4. Data acquisition and analysis parameters per reconstruction (recon) for specimens from sample f.

recon			ROI 1			ROI 2			DR	DE	ICF	L_R	S/C	ID
	T	PE	N	Ga	In	N	Ga	In						
11	54	2	57	40	2.9	57	40	3.2	0.4	0.3	2.0	40	1.08	6-2_01208v04
12		5	57	41	2.8	56	41	2.8				50	1.15	6-3_01211v04
13(a)		10	54	44	3.2	54	43	3.5				42	1.10	6-5_01216v02
13(b)			53	44	3.1	NA						NA		…v03
13(c)			51	46	3.3	51	45	3.6				40		…v04
13(d)			51	46	3.3	NA						NA		…v05
14		50	47	50	3.7	49	47	3.7				26	1.09	6-6_01215v03
15		100	39	57	3.7	45	51	3.6				41	1.11	5-6_01217v03
16		1000	9	86	5.6	10	85	5.7				35	1.04	5-5_01218v02

Both ROI cylinders are placed just below the upper GaN/InGaN interface, are coaxial with the TLROI, overlap only the InGaN layer, and are of length L_R per recon. Comparative FESEM images of the tip before and after APT data acquisition are used in setting the scale for L_R. ROI 1 encloses the TLROI to the length indicated and ROI 2 is 20 nm in diameter. Abbreviations and labeling schemes are consistent with Table 3.

Table 5. Data acquisition and analysis parameters per reconstruction (recon) for specimens from sample d.

recon		ROI 1				ROI 2			DR	DE	ICF	S/C	L_R	ID
	T	PE	N	Ga	In	N	Ga	In						
17	54	2	56	42	1.5	54	44	1.2	0.4	0.27	2.0	1.00	155	1-1_01093v03
18(a)		10	50	48	1.6	51	48	1.7				1.16	220	1-2_01096v01
18(b)			51	48	1.5	NA							NA	…v02
18(c)			49	50	1.6	51	47	1.7					220	…v03
18(d)			49	50	1.6	NA							NA	…v04
19		100	33	64	2.2	44	54	2.0		0.28		1.07	128	1-3_01097v04
20		1000	6.1	91	2.7	11	87	2.8		0.20		1.30	133	1-4_01098v04

ROI placements, diameters, and scaling are consistent with Table 4. Abbreviations and labeling schemes are consistent with Table 3.

Table 6. Data acquisition and analysis parameters per reconstruction (recon) for specimens from sample c.

recon		ROI 1				ROI 2			DR	DE	ICF	S/C	L_R	ID
	T	PE	N	Ga	In	N	Ga	In						
22	54	2	57	42	1.4	56	42	1.5	0.4	0.22	2.00	1.13	62	1-1_01220v03
23		5	52	46	1.5	53	45	1.6		0.28		1.22	37	1-1_01221v02
24(a)		10	47	51	1.5	52	46	1.6		0.29		1.11	38	1-3_01222v04
24(b)			48	50	1.6	NA							NA	…….v05
24(c)			47	52	1.6	50	48	1.7					38	…..v06
24(d)			47	52	1.6	NA							NA	….v07
25		50	34	65	1.8	48	51	1.5		0.20		1.23	44	1-4_01223v02
26	26	2	55	44	1.4	54	44	1.6	0.4	0.28		1.10	65	1-3_01227v03
27		5	52	47	1.5	53	46	1.7		0.21		1.09	50	2-2_01226v02
28		10	49	50	1.4	51	47	1.5		0.25		1.12	45	2-1_01225v02
29		50	37	61	2.0	47	51	1.7		0.29		1.17	46	1-6_01224v04

ROI placements, diameters, and scaling are consistent with Table 4. Abbreviations and labeling schemes are consistent with Table 3.

We now present some detailed cases from sample h. Figures 2(a—c) illustrates the evolution of the specimen tip of recon 1, which shows: (a) the FIB-prepared tip that supports a thin Ni capping layer, (b) the resulting tip after the Ni cap and a portion of the GaN top layer have been field-evaporated away, and (c) the remaining tip after the InGaN layer, and a portion of the underlying GaN layer, have been field-evaporated away. Estimation of S/C for this tip is thus obtained from Fig. 2(c). The range and variation in tip voltage (SV) corresponding to the data used recon 1 is given in Fig. 3, and the aggregate mass spectrum for all the ions accumulated over the same voltage range is shown in Fig. 4 (a).

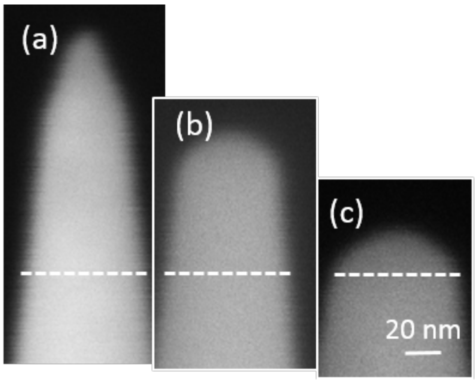

Figure 2

FESEM images showing the progression of tip evolution for the specimen used in recon 1. (a) Tip after FIB processing completed. The tip apex is composed of residual Ni (from the FIB preparation process) that is ≈ 20 nm thick. (b) Remaining tip after all of the Ni and a portion of the GaN capping layer have been removed by APT. (c) Tip after the remaining GaN capping layer, all of the InGaN layer, and a portion of the GaN template have been removed by APT. In (a) the tip tilts toward the observer and stands 54° from the horizontal; in (b) and (c) the tip is viewed as standing upright at an angle of 90° from the horizontal.

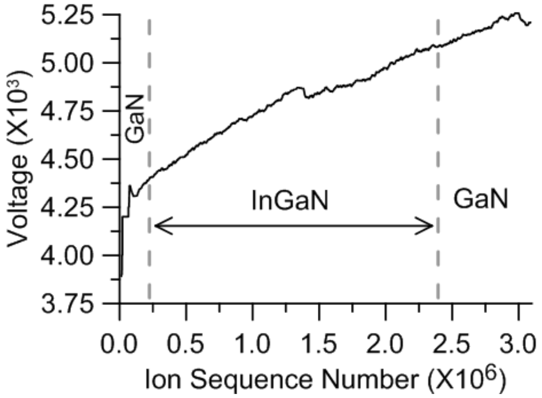

Figure 3

Variation in specimen voltage for the case of recon 1. The data acquisition starts with the status of the specimen tip as shown in Fig. 1(b) and ends with the status of the tip as shown in Fig. 1(c).

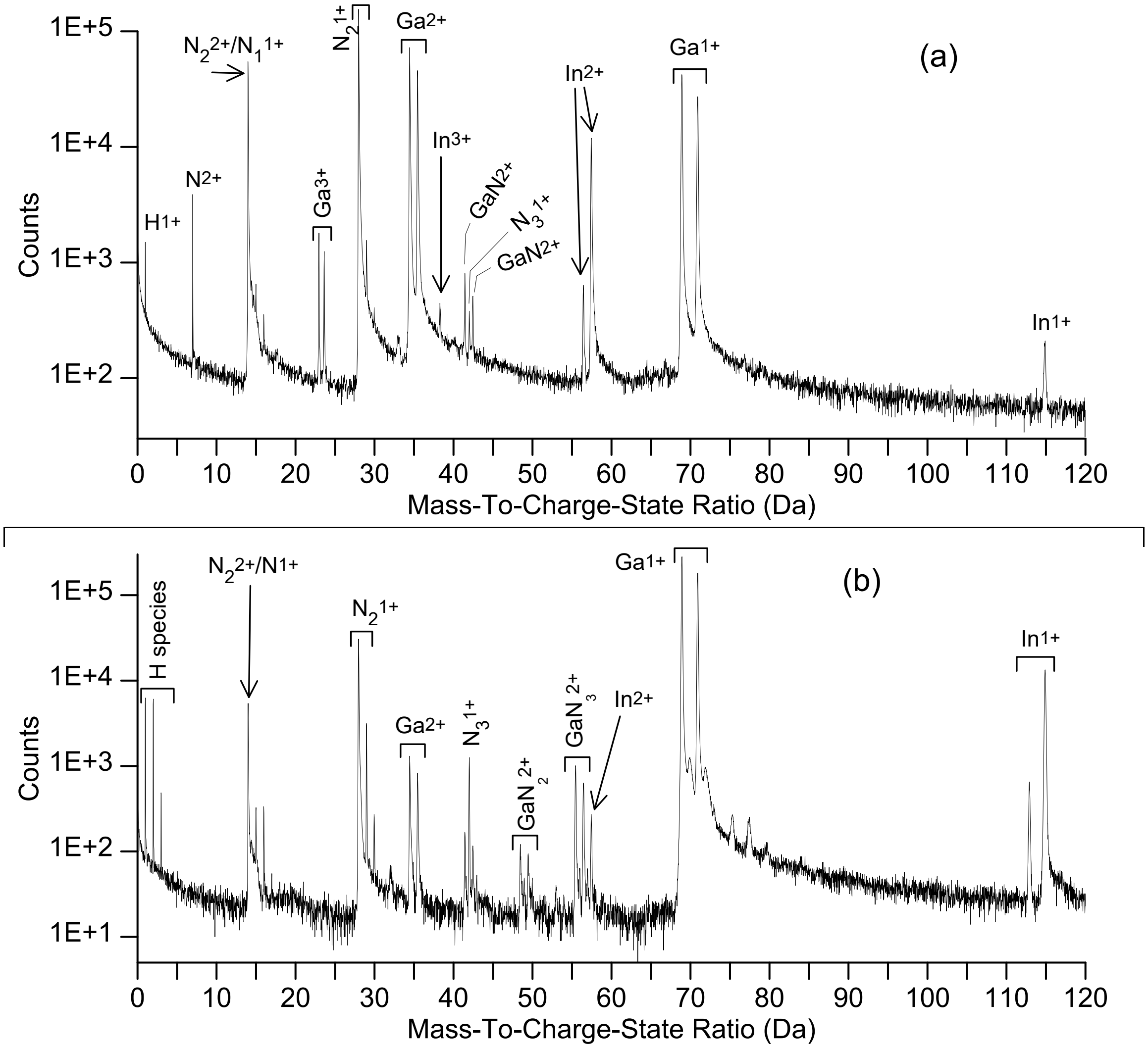

Figure 4

Fig. 4 (a). Accumulated mass spectrum corresponding to the TLROI of recon 1 (sample h, PE = 2 fJ). The peak assignments at 14 Da, 14.5 Da, and 15 Da are ambiguous and may arise variously from contributions of N^{1+} and N_2^{2+}. We assign the nearby minor peaks, extending to 16 Da, to N_xH_y molecular ions. Of course, a 16-Da peak could also arise from O^{1+} and/or O_2^{2+}, but that possibility is excluded in the present paper. (b) Full accumulated mass spectrum corresponding to the TLROI of recon 6 (sample h, with PE = 1000 fJ). Compared to (a), there is an increased presence of H species and molecular ions of N_xH_y, N_3, GaN_2, and GaN_3. Additionally, compared to (a), the Ga^{1+} and In^{1+} charge states are more prominent than their respective 2+ charge states. Labels on the various minor peaks are omitted for clarity.

Further details of recon 1 are now presented. Figure 5(a) shows the 3D atomic map illustrating the InGaN layer embedded between top and bottom GaN regions. In IVAS nomenclature, this map is the “top-level ROI” (TLROI), which incorporates all ions collected over the voltage span utilized. With parameters indicated in Table 3, IVAS simultaneously renders both InGaN/GaN interfaces as approximately planar and parallel; the IVAS-derived InGaN layer thickness is within ≈ 1 nm of the result obtained by XRD. The InGaN layer appears tilted with respect to the z axis because FIB processing variations prevented a more nearly perpendicular orientation of the specimen tip. Figure 5 (a) illustrates that the TLROI may be represented by the IVAS software either in detector view or specimen view; these distinctions were described earlier.

A graph of the 1D, TLROI, z-axis concentration profile for Ga, N, and In, corresponding to Fig. 5(a), is shown in Fig. 5(b); the Ga/In transitions appear artificially graded, which results from the tilted orientation of tip as just described. Figure 5(b) also illustrates a non-physical, N-rich composition of both the top and bottom GaN layers. Figure 6(a) shows a 20-nm-diameter, cylindrical ROI that subdivides the TLROI; a z-axis concentration profile constrained to this ROI is shown in Fig. 6(b). The results illustrated in Figs. 5(b) and 6(a, b), and listed in Table 3 for this PE = 2 fJ case, indicate that the APT derived concentrations for In, N, and Ga within the InGaN layer are rather insensitive to ROI diameter. On the other hand, the measured concentrations for Ga and N in the GaN regions are comparatively dependent upon the geometry of the ROI. We now explore concentration profiles along ROI axes oriented perpendicular to the TLROI *z*-axis of recon 1.

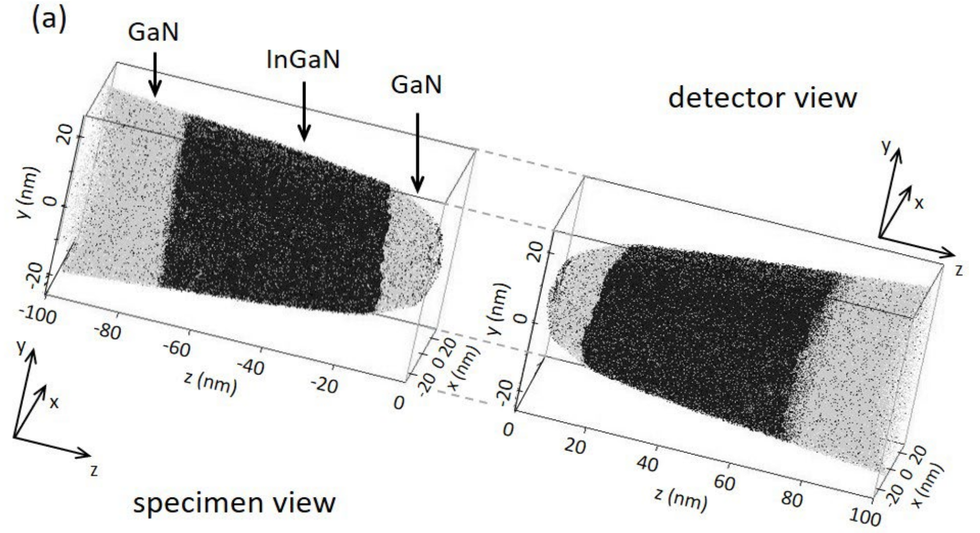

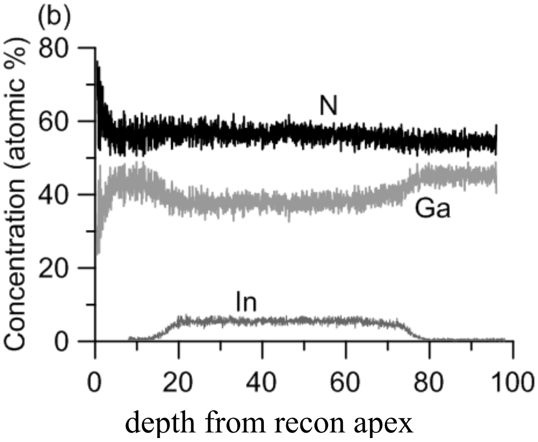

Figure 5

Recon 1. (a) The InGaN layer, a remnant of the GaN capping layer, and a portion of the GaN template are shown in this TLROI. Due to FIB processing errors, the long axis of the tip is tilted somewhat with respect to the normal of the GaN/InGaN interfaces and thus the InGaN layer appears tilted. The coordinate system shown illustrates the IVAS-defined recon conventions for both specimen view and detector view. The specimen view conforms to the true, physical orientation of the tip. The detector view maintains the physical x and y coordinate orientations but inverts the z coordinate. (b) Depth dependent concentration profile of the TLROI for In, Ga, and N is measured (along z) from the recon apex—and thus appears the same in either specimen view or detector view. The first several nm of apparent In concentration are omitted since In is insignificantly present in the capping layer. At the 2 fJ PE used for this case, the measured stoichiometry of the GaN template region is (non-physically) N-rich with the recon apex portion showing an even more pronounced effect. Note that the recon apex does not generally conform to the apex of the physical tip at the start of an APT data acquisition run. This is because numerous ion counts from the start of the run are often excluded from the recon since they are consumed in the time required to align the tip and set the laser focus before data acquisition can proceed in a controlled manner.

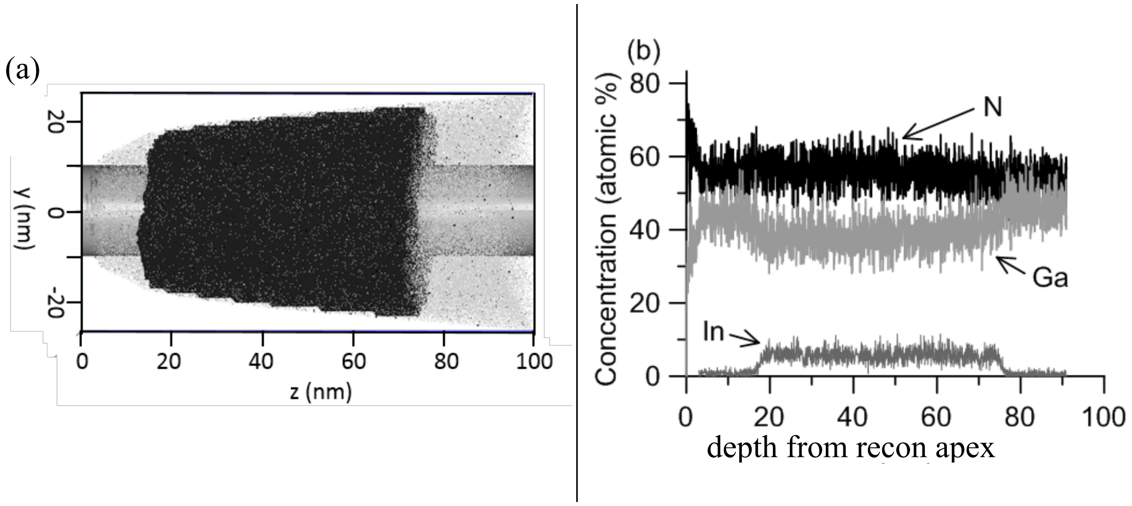

Figure 6

(a) A 20-nm-diameter cylindrical ROI aligned coaxially with the TLROI of recon 1 shown in detector view. The z-axis of the ROI is collinear with the z-axis of the TLROI. (b) Depth dependent concentration profile (along z), as measured from the recon apex, for In, Ga, and N in the cylindrical ROI shown in (a). Within the confines of the cylindrical ROI, the apparent, non-physical, N-rich stoichiometry of the GaN template layer is less pronounced than in Fig. 5(b).

Figure 7 shows a 2D relative-density map for Ga that exhibits 6-fold rotational symmetry (about z). This map is derived from recon 1 and plotted in the coordinate system of the reconstruction such that the relative density of Ga is projected onto the *x*-*y* plane at the maximum z-coordinate of the TLROI. Thus, given the z-axis convention shown in Fig. 5 (a) for both specimen view and detector view, the 2D map will appear the *same* in either view. Maps analogous to Fig. 7 were noted as revealing the 6-fold symmetry of the ⟨0001⟩ zone of the III-N wurtzite lattice.[9] We use Fig. 7 to place two cuboid-shaped ROIs (ROI A and ROI B), both oriented perpendicular to *z*, and both intersecting the TLROI as illustrated in Fig. 8. ROIs A and B are placed to intersect regions of high and low relative Ga density, respectively. The dimensions of these ROIs are indicated in the associated figure captions. Figures 9 (a, b) show that the comparative axial concentration profiles (for N, Ga, and In) along A and B (within the cuboids) are nearly equal—regardless of what Fig. 7 may suggest to the contrary. However, as described next, these effects are complex and the spatial distribution of measured composition can depend upon PE, the ionic charge state represented, and may not reveal any underlying crystal symmetry whatsoever.

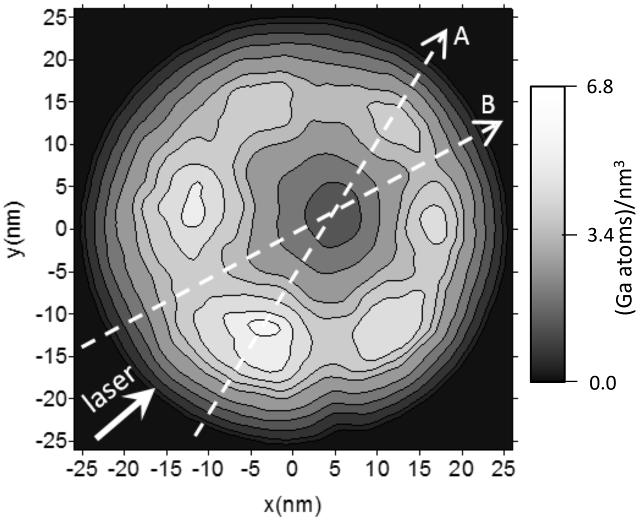

Figure 7

2D relative density plot for Ga as projected onto the *x-y* plane of recon 1. White indicates relative maximum Ga density and black indicates zero density. This is the default rendering of the IVAS software with no additional smoothing. The map serves as a guide with which to orient ROIs as discussed in the following figures. In the coordinate convention shown, the laser is incident from the lower left and the plot illustrates a 6-fold rotational symmetry similar to prior work.[9] Dashed lines A and B indicate the orientation of respective ROIs that are further illustrated in Fig. 8 with A intersecting regions of relatively high Ga density and B intersecting regions of relatively low Ga density. The displacement of the center of the plot in the positive *x-y* direction arises from the accidental tilt of the tip in FIB mounting.

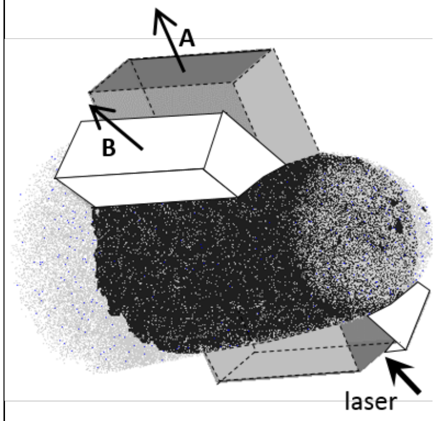

Figure 8

The InGaN portion of recon 1 intersected by ROIs A and B, as identified by their respective long axes as shown. Both A and B are cuboids and both have dimensions 75 nm × 45 nm × 15 nm.

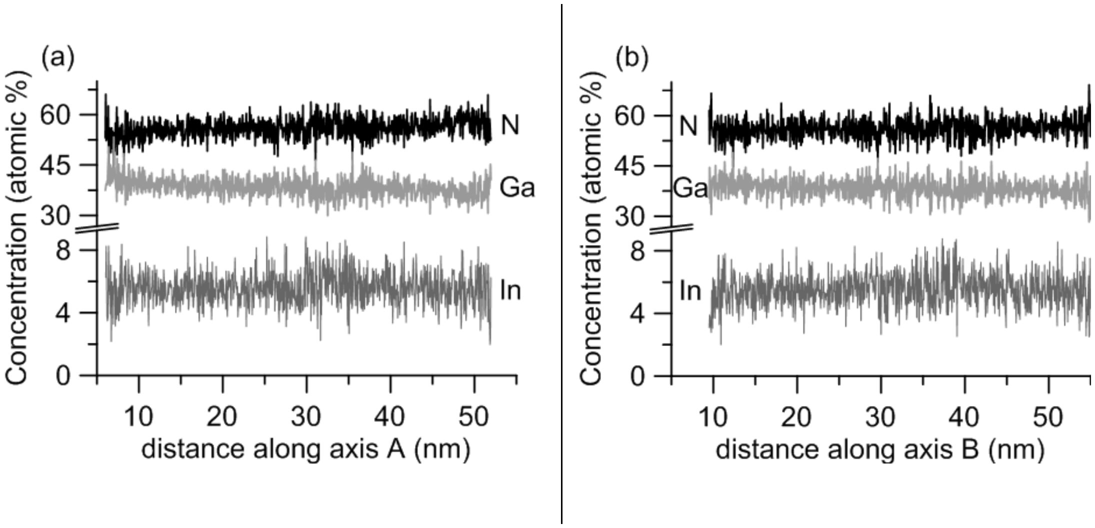

Figure 9

Axial concentration profiles for N, Ga, and In confined to ROIs A and B as shown in Fig. 8. The respective concentration profiles contained in ROI A and B are illustrated in (a) and (b) above. The results indicate that for recon 1 with PE = 2 fJ, the concentration profiles are nearly constant and essentially independent of the azimuthal placement of the ROIs.

The data of Fig. 9 (a) is recast in Fig. 10 (a, b) to illustrate the 1D concentration profiles for the prominent charge states observed for Ga and In. Recasting Fig. 9 (b) yields similar results, which are omitted for brevity. Figure 10 (a) shows the concentration profile of Ga^{1+}, and the combined profiles of Ga^{2+} with Ga^{3+}. Notably, Ga^{1+} falls nearly to zero in the center. Ga^{1+} and $Ga^{2,3+}$ vary with similar magnitudes, but in opposition, such they add up to the relatively uniform Ga concentration profile shown in the graph of Fig. 9 (a). A similar complementary trend for In^{1+} and $In^{2,3+}$ is shown in Fig. 10 (b), but in this case (PE = 2 fJ) the In^{1+} contribution is comparatively minor.

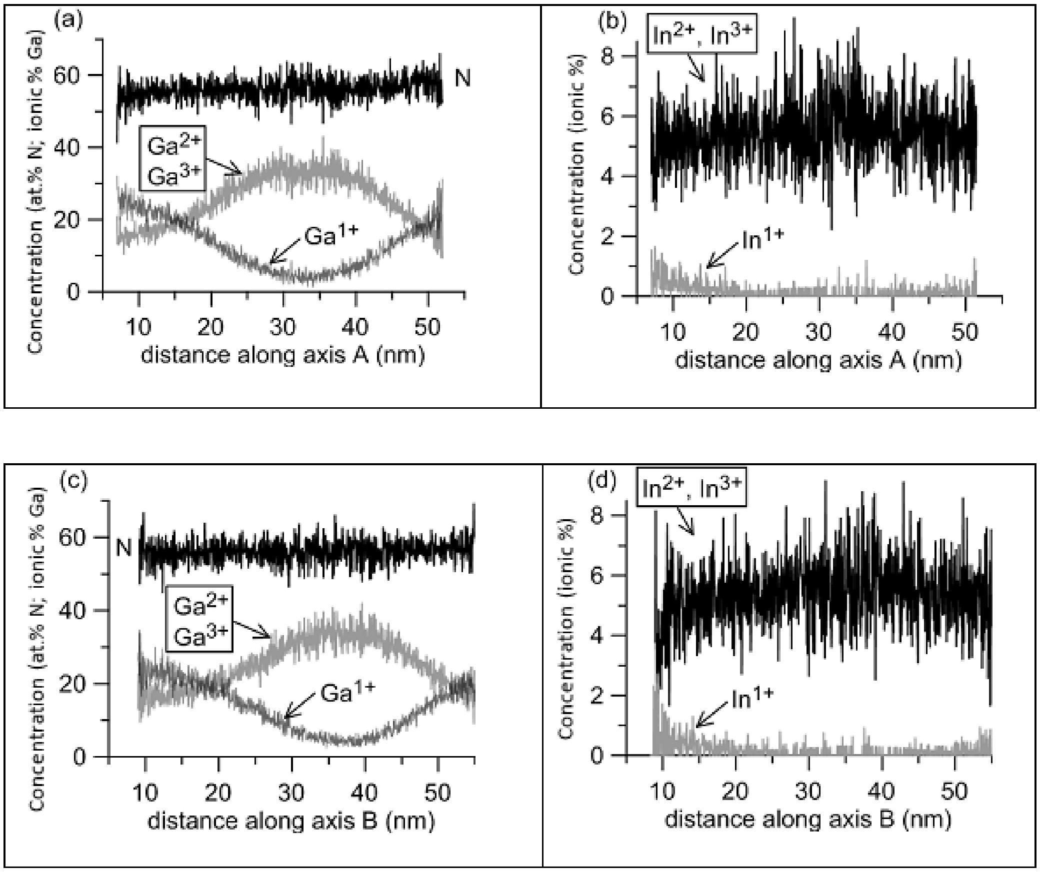

Figure 10

Concentration profiles in ROIs A and B of Fig. 8 for various charge states of Ga and In. Again, PE = 2 fJ. (a) The radial dependence of the Ga charge states in ROI A reveals that the combined Ga^{2+} and Ga^{3+} concentrations attain a maximum near the center of the reconstruction with the Ga^{1+} concentration displaying the opposite spatial behavior. Interestingly, the radial dependence of the sum of all 3 Ga charge states results in the nearly uniform concentration profile for Ga as illustrated in Fig. 9 (a). (b) Concentration profiles for the 3 observed charge states of In in ROI A showing that In^{1+} is essentially negligible and the combined concentrations of In^{2+} and In^{3+} show relatively weak radial dependence. (c) Similar to (a) but confined to ROI B. (d) Similar to (b) but confined to ROI B. The rightward displacement of the $Ga^{1+2+,3+}$ extrema in (a) and (c) arise from the accidental tilt of the tip in FIB mounting.

We now survey the results of recon 3(a) for the case of PE = 10 fJ. Figure 11 (a) shows the TLROI (in detector view) intersected by axial and diametric ROI cylinders, *a* and *d*, respectively, which are each 20 nm in diameter. Figs. 11 (b—d) show graphs of the respective 1D concentration profiles in ROI *d*, the TLROI, and ROI *a*. Figs. 11 (c, d) both indicate nonphysical composition trends for N and Ga, but the effect is more pronounced for the GaN region of Fig. 11 (c). Figures 11 (b, d) both illustrate that roughly stoichiometric Ga and N fractions are found in the GaN region when the analysis is constrained to ROI *a*.

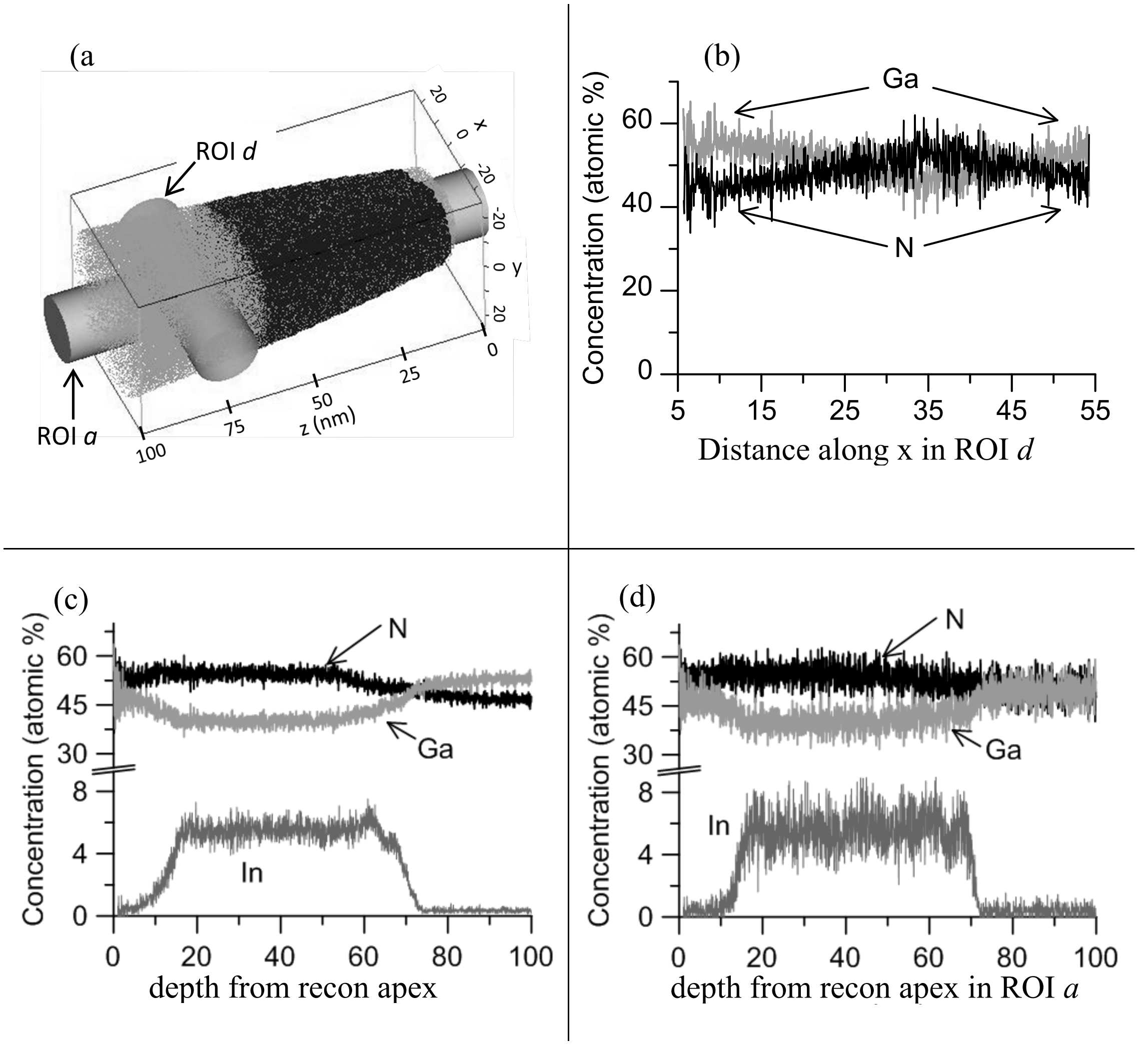

Figure 11

Concentration profiles for recon 3(a) with PE = 10 fJ. (a) TLROI with axial and diametric ROI cylinders *a* and *d*, which are each 20 nm in diameter. The InGaN layer appears in black and the GaN sublayer, and remnant of GaN capping layer, appear in gray. ROI *a* intersects the capping, InGaN, and sublayers while ROI *d* resides entirely in the GaN sublayer. (b) Concentration profiles for Ga and N in ROI *d*. These data illustrate that, on average, IVAS will yield approximate GaN stoichiometry within a 20 nm diameter region bracketing the Ga and N extrema. (c) Concentration profiles within full TLROI showing apparent Ga-rich composition within the lower GaN layer, which is consistent with the trend shown in (b). (d) Concentration profiles in ROI *a*. Here, the GaN composition in the sublayer appears roughly stoichiometric as expected from (b). Both (c) and (d) indicate non-physical variations in N concentration in going between the InGaN and GaN layers, i.e., the ideal N concentration should remain at 50 at. % throughout.

In a similar manner as just discussed, Figs. 12 (a, b) compare concentration profiles between the TLROI and a 20-nm-diameter, coaxial ROI cylinder for the case of recon 5 with PE = 100 fJ. The deviation from stoichiometry in the GaN region is quite pronounced in both cases. However, the 4 examples illustrated in Figs. 11 (c, d) and 12 (a, b) indicate that the indium concentration is comparatively insensitive both the ROI selection and PE.

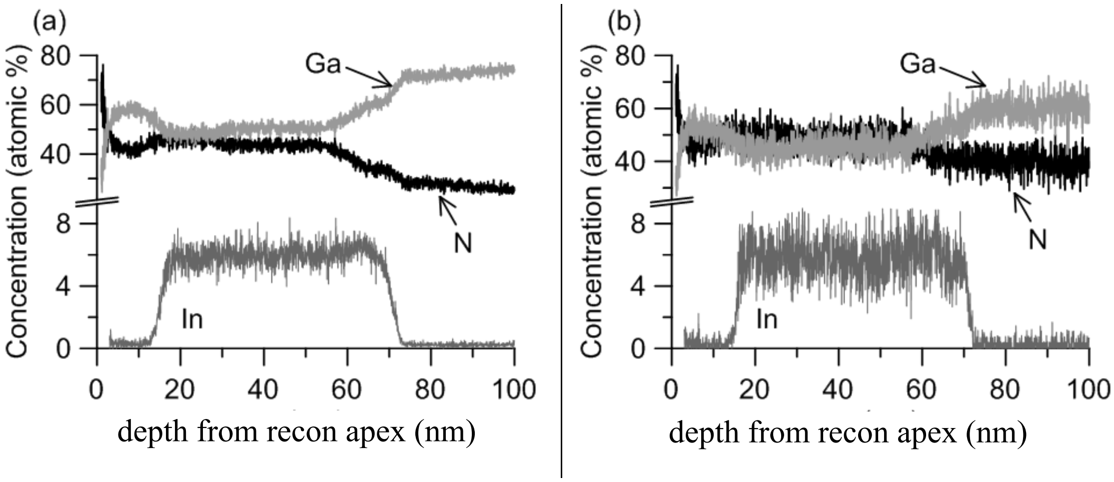

Figure 12

Axial concentration profiles of N, Ga and In for recon 5 with PE = 100 fJ. (a) Concentration profiles within the full TLROI showing measured Ga-rich composition within the GaN layers. (b) Concentration profiles confined to a 20 nm diameter ROI cylinder placed coaxially with the TLROI. In this case the composition also appears Ga-rich in the GaN layers. Both (a) and (b) indicate non-physical variations in N concentration in going between the InGaN and GaN layers.

Figures 13 (a, b) illustrate transverse concentration profiles for recon 5 for the case of PE = 100 fJ. The ROI is denoted by “A” and has the same dimensions, and approximate orientation (with respect to the laser input) as for the transverse ROI (pertaining to recon 1) shown in Fig. 8. For this case, however, the corresponding 2D map of relative Ga density shows an approximately radially symmetry; the 6-fold azimuthal feature, as seen in Fig. 7, is not evident for recon 5. Hence, for Figs. 13 (a, b), “radial concentration fluctuations” and “transverse concentration fluctuations” are synonymous. Figure 13 (a) illustrates that both Ga^{1+} and Ga^{2+} are detected, but Ga^{1+} is the dominant specie. The net Ga concentration is not radially uniform but is lower at the center of the TLROI than at the sidewalls. The radial variations of the In^{1+} and In^{2+} concentrations appear in Fig. 13 (b); the In^{3+} charge state was not detected. Interestingly, and in contrast to the case of recon 1, Fig. 13 (b) illustrates that the radial concentration fluctuations of the indium species are of similar magnitudes, but in opposition, such that the net transverse indium concentration adds up to be roughly uniform. Similar results are found in Fig. 14 (a, b) that pertain to ROI “B”.

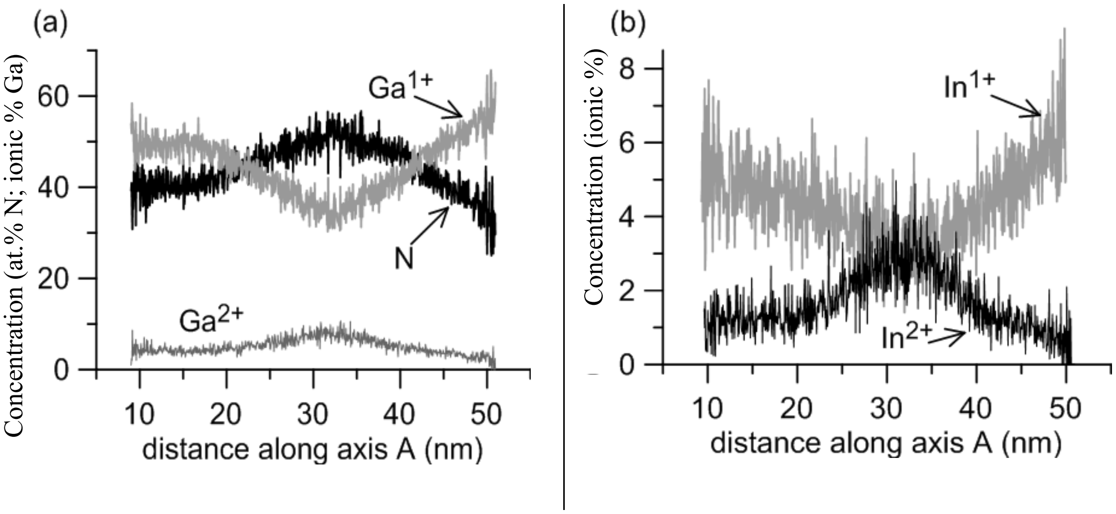

Figure 13

Concentration profiles for N, Ga, and In for ROI A placed into the InGaN portion of recon 5 where PE = 100 fJ. Here, the ROI has the same dimensions and orientation in the TLROI as was described for the corresponding ROI of Fig. 8. However, in contrast to the example shown in Fig. 7, the present case with PE= 100 fJ revealed only approximate radial symmetry of the measured Ga density; no 6-fold azimuthal symmetry was observed. Therefore, to maintain consistency with Figs. 7 and 8, ROIs A and B (see Fig. 14) are oriented with respect to the laser direction and not to the relative Ga density. (a) Concentration profiles for Ga^{1+} and Ga^{2+} are expressed in ionic %, and N in atomic %. For this case, both the N and Ga^{2+} concentrations peak at the center of the ROI, but Ga^{2+} is a minor contribution to the total Ga ionic concentration; Ga^{3+} is negligible and not shown. (b) Concentration profiles of In^{1+} and In^{2+} are also expressed in ionic % and illustrate that In^{2+} peaks in the center of the ROI and the summed concentrations result in an approximately constant total indium concentration within the ROI.

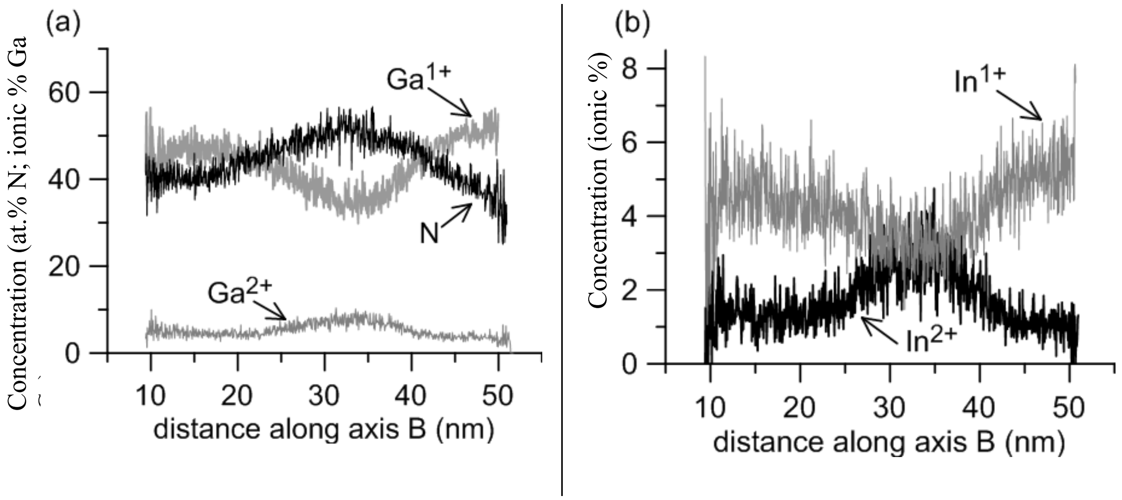

Figure 14.

Concentration profiles for N, Ga, and In for ROI B placed into the InGaN portion of recon 5 where PE = 100 fJ. The ROI has the same dimensions and orientation in the TLROI as was described for the corresponding ROI of Fig. 8 and it is placed with respect to the incident laser direction as described in Fig. 13. (a) Concentration profiles for Ga^{1+} and Ga^{2+} are expressed in ionic %, and N in atomic %. (b) Concentration profiles for In^{1+} and In^{2+} are expressed in ionic %. The results are comparable to those illustrated in Figs. 13 (a, b).

The results for sample h surveyed in Figs. 5—14 illustrate that the 2D distribution of atomic composition, and the charge states of individual species, depend on PE and correlate with the variation of the electric field strength over the specimen apex for a given SV and tip geometry. In our usage, "surface field" or "surface electric field" synonymously refer to the electric field on the vacuum side of the tip-vacuum interface and is abbreviated as E_s. Based on the Kingham post-ionization theory [34] as applied to APT analysis of III-Nitrides, the observed CSRs of the detected Group-III ionic constituents can be directly related to E_s such that increased surface field results in increased relative yield of the 2+ ionic species.[7] Therefore, the observed transverse concentration profiles for Ga^{1+}, Ga^{2+}, In^{1+} and In^{2+}, and their respective CSRs, described in the foregoing discussion, can be regarded as transverse spatial indicators of E_s across the surface of the tip such that maximum in Ga^{2+} and/or In^{2+} counts should occur at the geometrical apex. Indeed, as pointed out by Mancini, et al.[7], "It thus becomes possible to establish microscopic relationships between the local surface field and the locally measured composition. The local surface field can be related to local composition." However, it should be clarified that the Kingham theory infers an "effective" surface field, based on measurements of CSR and does not actually associate measured CSRs with the physical field E_s. In Section 4, we discuss the direct calculation of the E_s for a representative GaN specimen tip under realistic APT conditions.

To summarize the results for the *c*-plane samples: The key trends that emerge from analysis of sample h (Table 3) are: (i) The measured concentration of indium increases with increasing PE. (ii) There is no significant difference between the indium concentrations computed for the two temperature cases. (iii) PE in the approximate range of (2—50) fJ will produce indium concentrations that are within experimental error of the RBS results. (iv) Ranging 14 Da as N^{1+} instead of N_2^{2+} serves to fractionally increase the relative Ga and In counts per PE case, but this is not significant within the uncertainty of the RBS measurements. (v) Choice of single or multiple detection events does not significantly change the results. (vi) Analysis confined to the 20 nm diameter ROI cylinders will return results closer to stoichiometry for the GaN sections of the specimens, but the In concentration is comparatively insensitive to ROI diameter. The trends that emerge from analysis of samples f, d, and c (Tables 4—6) are similar to the trends just described except that the respective PE ranges yielding results within the RBS uncertainty are (2—10) fJ, (2—100) fJ, and (2—50) fJ.

3.1.2. *m*-plane GaN/$In_xGa_{1-x}N$/GaN QW samples

These QW specimens were comparatively fragile and fractured easily during APT. Thus, it was not feasible to accumulate a wide range of PE cases that would simultaneously render all 3 QWs as illustrated if Fig. 1(b). Additionally, the GaN capping layer was ≈ 5 nm thick and provided little material for the preliminary tip-formation during the alignment phase of APT data acquisition. Therefore, the top-most QW was often consumed during the alignment process, or had been partially milled away by the FIB, and only the bottom two QWs usually provided useful data. Furthermore, the nature of these specimens, as derived from arrays of *c*-axis grown GaN/InGaN core-shell microposts, precluded RBS analysis. Nevertheless, it is instructive to compare APT performed on these *m*-plane, core-shell QW samples to the results obtained from thicker, c-plane, “bulk like” InGaN layers. It is also instructive to compare these core-shell specimens with prior APT work on planar, *m*-plane GaN material as reported by other workers.[22]

Table 7 lists details of APT analyses of three representative cases for the core-shell QW specimens. PE= 10 fJ in recon 30 and all 3 QWs were recovered. In recons 31 and 32 the respective PE values were 15 fJ and 20 fJ and only the lower 2 QWs were recovered for those cases. The listed IVAS fitting parameters were selected as compromises to approximately duplicate the TEM-determined separation between the 1st and 3rd QWs for recon 30, the separation between the 2nd and 3rd QWs for recons 31 and 32, and render QW layers as approximately planar in each case. As discussed next, simultaneously meeting these constraints in the reconstruction analysis, even for QW layers that are comparatively thin and closely spaced as these were, is usually not achievable.

Table 7. Data acquisition and analysis parameters per recon for specimens from m-plane samples.

recon	T	PE	QWs in recon	DR	DE	ICF	S/C	L_R	ID and notes
30	54	10	1, 2, 3	0.3	0.46	2.0	1.06	80	2-2_02097v07 (QWs tilted in recon)
31		15	2, 3	0.4	0.50	2.0	1.20	40	1-3_01468v02 (QWs tilted in recon)
32		20	2, 3	0.3	0.25	2.3	1.40	90	1-2_01465v03 (QWs show less tilt)
33		10	no QWs present	0.3	0.20	2.0	1.10	120	2-3_02095v03 (GaN only)

As described in the text, the GaN capping layer was comparatively thin and therefore the topmost QW (QW 1) was often consumed in the process of tip alignment. QW 1 was thus unavailable in recons 31 and 32. For the case of these *m*-plane samples, L_R refers to the length of the TLROI and the scale was set by forcing the recons to simultaneously render the QWs as approximately planar and separated by the TEM-determined spacing. Hence, L_R does not typically conform to the true total length of material removed from the tip—as measured by FESEM before and after data acquisition. Due to FIB milling errors, recon 33 has no QWs present but is included to illustrate consistency of the asymmetric tip evolution artifact found in *m*-plane specimens. For recon 33, L_R is estimated by comparing FESEM images recorded before and after APT and the apparent disparity between DE for this case and recon 30, which used the same PE, arises from the difficulty in estimating L_R from FESEM images when no QW layers are present to serve as markers.

Figure 15 (a) shows the TLROI (in detector view) for recon 30 and reveals two recurring problems: (i) FIB processing issues have again yielded a tip that is tilted with respect to the QW layers, (ii) the IVAS software does not simultaneously render the 3 QWs as approximately planar. Similar issues were encountered for other reconstructions (not shown) of this sample, i.e., a tilted tip and not-simultaneously-planar QWs. Figure 15 (a) also shows a 15-nm-diameter ROI cylinder, placed roughly perpendicular to the QWs, and Fig. 15 (b) shows the 1-D concentration profile along the axis of this ROI. Taken together, these results again show that the IVAS fitting parameters, reconstructions, and the placement and diameters of the cylindrical ROIs, represent compromises in efforts to duplicate the TEM-determined QW separations and render approximately planar layers. Comparatively speaking, considering all samples examined in this study, it was quite unusual that (roughly) planar and parallel interfaces *could* be rendered for sample h as illustrated in Fig. 5(a).

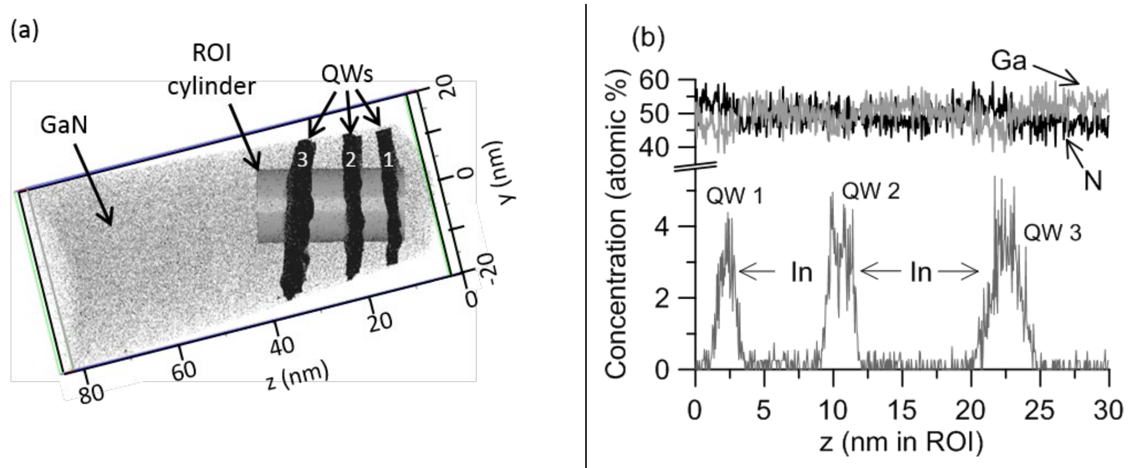

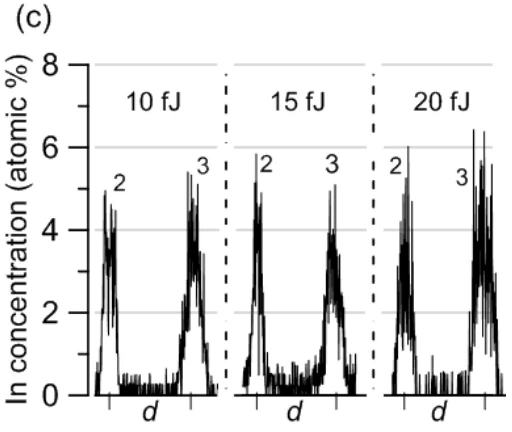

Figure 15

(a) TLROI (in detector view) of recon 30 for *m*-plane sample with PE = 10 fJ. The three QWs are highlighted with isoconcentration surfaces for indium set to 1.0 at. %. The QWs appear tilted with respect to the reconstruction z-axis because of FIB processing issues. An ROI cylinder (15 nm diameter) is placed centrally with respect to the x-axis and tilted to accommodate the tilt of the QW. (b) Axial concentration profiles for Ga, N, and In along z-axis (long axis) of cylindrical ROI. (c) Comparative axial concentration profiles for In in the bottom two QWs for recons 30, 31, 32, with respective PEs of 10 fJ, 15, fJ and 20 fJ. The concentration profiles are computed within 15-nm-diameter ROI cylinders which are placed and tilted as described in (a). The reconstruction parameters are chosen to yield the QW separation d ≈ 12 nm for each case. The results indicate that, for this range of PE, the measured PE-dependent variation of In concentration cannot unambiguously be distinguished from possible spatially-varying concentrations of In that occur during growth.

Figure 15(c) compares the z-axial, In concentration profiles generated within 15-nm-diameter ROI cylinders for the 2nd and 3rd QWs for the 3 PE cases of recons 30, 31, and 32. In each case, the ROI cylinders are oriented roughly perpendicular to the QW layers. The results of this (small) set of measurements suggest that there may a resolvable trend whereby increasing PE from 10 fJ to 20 fJ results in a corresponding fractional increase in measured indium concentration of roughly 10%. However, this cannot be unambiguously distinguished from possible spatial variations of In concentration that may occur between separate nanorods during growth. Photoluminescence was also used to separately estimate the QW alloy composition in these micropost samples and yielded $x \approx 0.10$, which, for this PE range, is consistent with APT studies of the *c*-plane samples.

Figure 16 illustrates a 2D relative-density plot for Ga that was generated under recon 32 with PE = 20 fJ. Recall that the relative-density plot will appear the same regardless of the recon being generated from either specimen view or detector view. In contrast to Fig. 7, however, Fig. 16 shows no azimuthally 6-fold rotational symmetry, but instead shows an in-plane, 2-fold axis of symmetry. Notably, the 2-fold feature is not “washed out” at the PE used. As discussed above, the 6-fold feature shown in Fig. 7 with PE = 2 fJ did not persist in recon 5 where the PE was 100 fJ, which illustrates that the appearance of these underlying symmetry features very much depends on the PE.

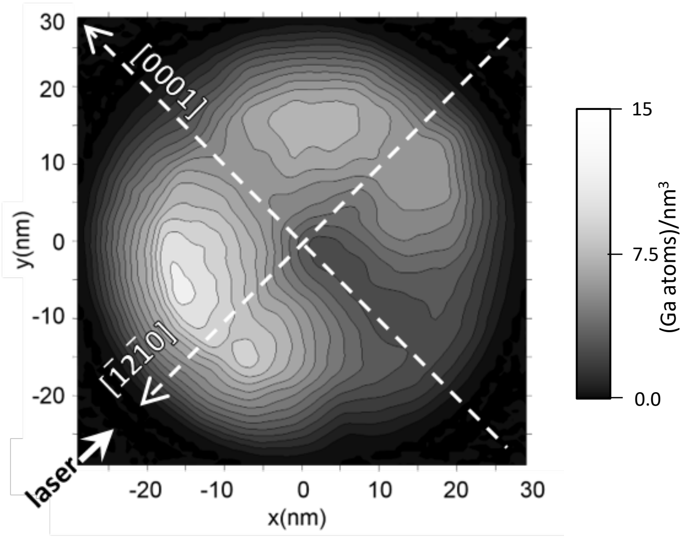

Figure 16

2D relative density map of Ga derived from the TLROI of recon 32 with PE = 20 fJ. The indicated axes are established as described in the text.

Recon 32 is useful to illustrate this 2-fold effect in relative Ga density since the tip had the least-tilted orientation, due to FIB mounting errors, with respect to the QW/GaN interfaces compared to all other core-shell specimens examined. Given our specimen lift-out and mounting convention, and the separately evaluated polarity of the core-shell nanoposts [28-30], the 2-fold axis shown in Fig. 16 conforms to the crystallographic *c*-axis of the sample with the [0001] direction as indicated. The 6-fold rotational ambiguity of a hexagonal lattice about the *c*-axis allow us to arbitrarily assign the $[\bar{1}010]$ direction of the tip as pointing toward the two-dimensional detector. Hence, the $[\bar{1}010]$ direction of an *m*-plane specimen tip is assigned to conform with the +z direction of an associated reconstruction. The correlation of the *c*-axis polarity with the character of the 2D map of Fig. 16 is consistent with that reported in Ref. [22]. The Miller-Bravais indexing convention for a hexagonal lattice may be found in the textbook by Cullity [35].

Figure 17 (a) illustrates the specimen-view, TLROI corresponding to recon 32. The figure also shows two ROI cylinders placed along [0001] and $[\bar{1}2\bar{1}0]$, respectively. Note that both ROI cylinders are 15 nm in diameter and intersect the TLROI only in the GaN region at a depth of roughly 50 nm below the deepest QW. Figure 17 (b) shows the axial concentration profile of Ga and N within the ROI along $[\bar{1}2\bar{1}0]$; Fig. 17 (c) show the concentration profile for Ga^{1+}, Ga^{2+}, and N along the same axis. Both graphs are essentially radially symmetric with respect to the TLROI. By contrast, as shown in Figs. 17 (d) and (e), the concentration profiles for Ga, N, Ga^{1+}, and Ga^{2+} for the ROI placed along [0001] are noticeably asymmetric. Figure 17 (f) shows the final state of the tip after the completion of the APT run and illustrates that the apex is displaced in the -*c* direction and away from the axial centerline of the tip. We now correlate these directionally dependent trends in CSR with both the symmetry of the tip and the strength of the surface electric field.

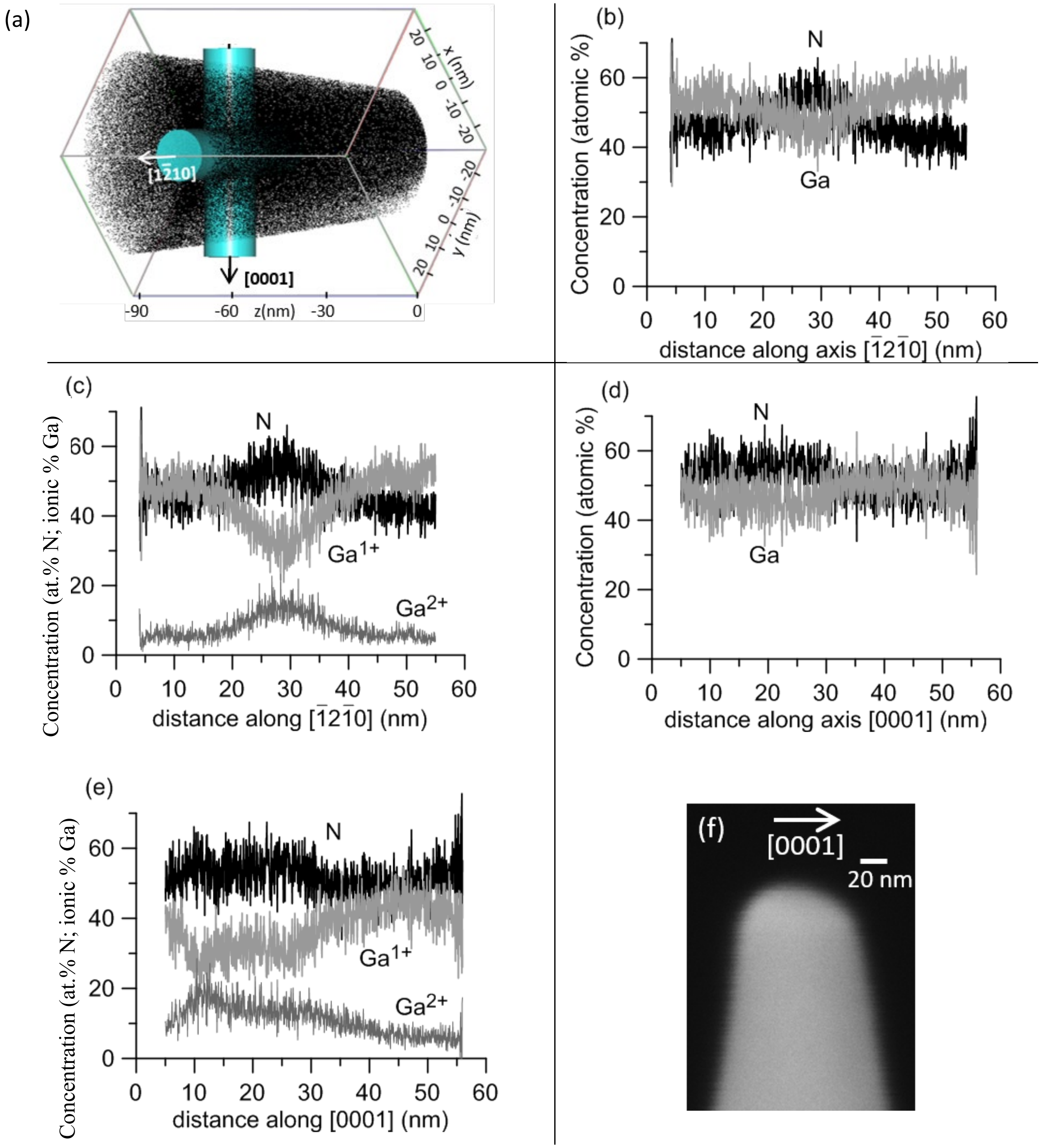

Figure 17

(a) TLROI of reconstruction 32 (specimen view) showing two ROI cylinders, each 15 nm in diameter, placed along the [0001] and [$\bar{1}2\bar{1}0$] directions, respectively. The ROIs encompass only GaN and are located roughly 50 nm below the QWs. (b) Concentration profiles for Ga and N within the ROI along [$\bar{1}2\bar{1}0$]. (c) Same as (b) but the Ga concentration, given in ionic %, is decomposed to show contributions of Ga^{1+} and Ga^{2+}. (d) Same as (b) but along [0001]. (e) Same as (c) but along [0001]. (f) Tip status after APT has removed all of the QWs. The tip evolves in the GaN with its geometric apex shifting toward -*c*.

By principles of basic electrostatics, the SV bias of a uniform GaN tip will produce a maximum surface field E_a at the tip apex.[36, 37] Therefore, the transverse concentration profiles for Ga^{1+} and Ga^{2+} can be regarded as transverse spatial indicators of the electric field strength across the surface of the tip with a maximum in Ga^{2+} counts occurring at the geometrical apex. This trend is indeed revealed in both *c*-plane and *m*-plane specimen tips but is most striking in *m*-plane specimens where it is radially asymmetric when viewed along [0001]. Specifically, when an *m*-plane tip is viewed in FESEM after APT analysis such that the [0001] axis is in the plane of the image, the resulting, quasi-hemispherical apex region is asymmetric, and the apex itself is displaced in the $[000\bar{1}]$ direction. Correspondingly, the relative concentration of Ga^{2+} is also spatially asymmetric and displaced in the $[000\bar{1}]$ direction. On the other hand, if a tip is viewed with a non-polar axis in the plane of the image, both the tip and the relative concentration profile of Ga^{2+} along that axis appear spatially symmetric. The tip evolution shown in Fig. 2, for a *c*-plane tip, combined with the associated graphs of Ga CSR of Figs. 10 (a, c), are representative of symmetric tip evolution.

However, an obvious caveat to keep in mind is that a tip will evolve asymmetrically for trivial cases when FIB processing inadvertently results in a tilted orientation. Using the IVAS software, such mounting errors can be immediately recognized as simply x-y displacements from symmetry of the 2-fold or 6-fold relative intensity maps for the respective *m*-plane and *c*-plane specimens. This effect can be seen in Fig. 7 for a slightly tilted FIB mounting of the *c*-axis tip since the center of the 6-fold feature is displaced in the positive *x-y* direction. On the other hand, the *m*-axis tip of Fig. 16 appears to be mounted without any significant tilt since the 2-fold map is symmetrically disposed. Hence, the correlation between apex evolution and *c*-axis orientation in *m*-plane specimens may be obscured and overlooked due to accidental FIB mounting artifacts.

A possible hypothesis to explain the asymmetric evolution of the m-plane tips is to associate it with the spontaneous polarization field $\vec{P}_S = -\hat{c}|\vec{P}_S|$, in units of C/m^2, which is known to exist in GaN. Values of $|\vec{P}_S|$ ranging from $0.007\ C/m^2$ to $0.034\ C/m^2$ have been reported.[38-40] In this convention, $\hat{c}$ is a unit vector directed along [0001] and $\vec{P}_S$ points from the Ga face toward the N face of the crystal. The magnitude of the electric field produced by this dipole is therefore (very roughly) $|\vec{P}_S|/\epsilon_o$ or ≈ (0.8—3.5) V/nm.[36, 37] Then, since we may estimate E_a to fall in approximate range of (10—20) V/nm [Ref. [3]], the dipole field would be a significant transverse perturbation to E_a. Therefore, the vector sum of these fields could compel the tip to evolve with an asymmetrically displaced apex as ions are field evaporated away. Although intuitively attractive, this viewpoint is dismissed in Section 4 where we illustrate that under typical bias conditions, the apex of the semiconducting GaN tip is generally in a state of inversion and the resulting density of mobile, free holes would screen any effect $\vec{P}_S$ would have on E_a. Instead, as discussed next, we propose that the asymmetric tip evolution is expected from growth habits, etch behavior, and Wulff plot analysis of *m*-plane GaN.[41-43]

Jindal, et al.[41] performed selective area growth of GaN on $(1\bar{1}00)$ GaN substrates and produced nanostructures with "arrow-headed shapes" such that the tip and base of an arrowhead point toward the [0001] and $[000\bar{1}]$ directions, respectively. The growth velocities in the $[000\bar{1}]$ and directions $[1\bar{1}00]$ are lower than that of the [0001] and $[1\bar{1}01]$ directions, producing a structure that is anisotropic in the *c*-direction. Consequently, as illustrated in Fig. 18, the geometric apex of such a nanostructure is displaced toward in the $[000\bar{1}]$ direction but the apex is symmetric with respect to the *a*-axis. Additionally, Megalini [42] has performed photo-electrochemical (PEC) etching of *m*-plane GaN structures and observed that the (0001) Ga face etches faster than the $(000\bar{1})$ N face. Taken together, these finding suggest that it is not unreasonable to expect that our *m*-plane APT tips should evolve in the asymmetric manner described previously and illustrated in Fig. 17 (f). Moreover, Fig. 18 also qualitatively suggests that when viewed with the *a*-axis in the plane of the image, the evolution of an *m*-plane tip should be symmetric, but also wider, than for the *c*-axis in the plane of the image. Figure 19 indeed suggests this trend for the case of the *m*-plane GaN tip of recon 33.

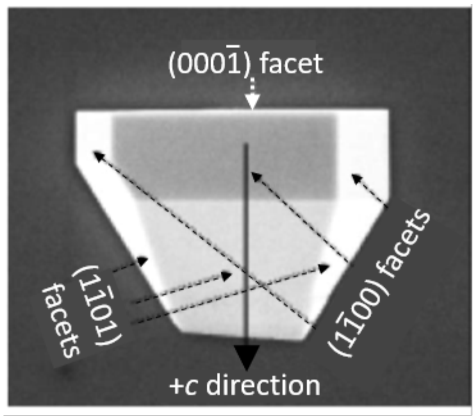

Figure 18

Growth habit of an *m*-plane, GaN structure as adapted from Ref. [41] and used with permission. The morphology of the structure, and the etching results of Ref. [42], lend credence to the hypothesis that the transverse shape of the APT tip should evolve asymmetrically with respect to the *c*-axis as illustrated in Fig. 17 (f) and Fig. 19 (a). The image also suggests that the transverse shape of the tip should evolve symmetrically with respect to the *a*-axis as shown in Fig. 19 (b).

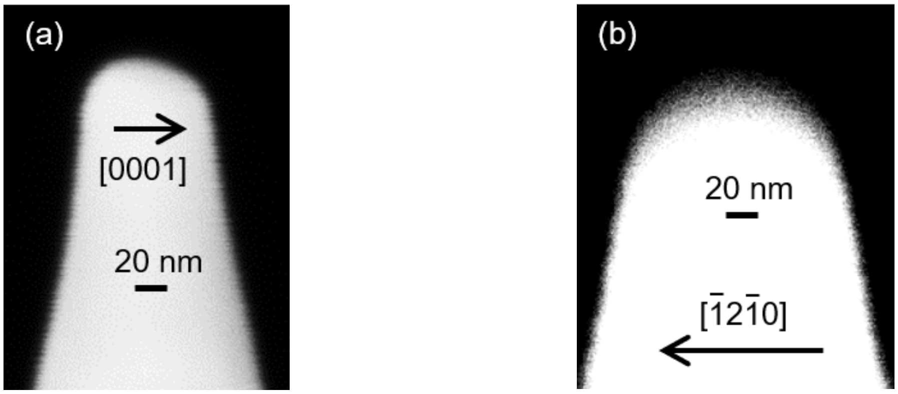

Figure 19

Orthogonal views of *m*-plane GaN tip from recon 33 after APT analysis. (a) *c*-axis in plane of image showing that the tip evolves such that apex is displaced in the -*c* direction, which is consistent with Fig. 17 (f). (b) *a*-axis in plane of image showing that the tip evolves symmetrically. The corresponding axial concentration profiles for these cases are quite similar to those shown in Fig. 17 (b—e) and are omitted for brevity.

4. Electrostatic analysis of GaN specimen tips

Our electrostatic analysis will consider only a representative case for the *m*-plane tip of recon 32 and examine only the GaN portion after the QWs have been field evaporated away. This abbreviated presentation is instructive and also puts into context application of what we refer to as the "*k*-factor" approximation [3] in computing E_a for semiconductor specimens tips. A more detailed exposition of our electrostatic analysis, and comparison with the *k*-factor approximation, is given elsewhere.[24]

A schematic of the tip-electrode geometry is given in Fig. 20. The key assumptions are as follows: The Si coupon and micropost are degenerately doped and treated as metallic conductors. The micropost stands 200 μm above the coupon and has the same taper as the FIB-milled specimen tip. As found from recon 32, the residual length of the GaN tip protruding from the Si micropost is ≈ 480 nm; this is the remainder of the tip after the quantum well layers have been removed. The tip apex diameter, as measured by FESEM following APT data acquisition, is ≈ 58 nm. For simplicity, the GaN tip is assumed to be ohmically bonded to the Si post. The nominal LE dimensions chosen and shown in Fig. 20 are adapted from other publications.[3, 44] The electrode-tip separation of ≈ 40 μm was experimentally estimated.

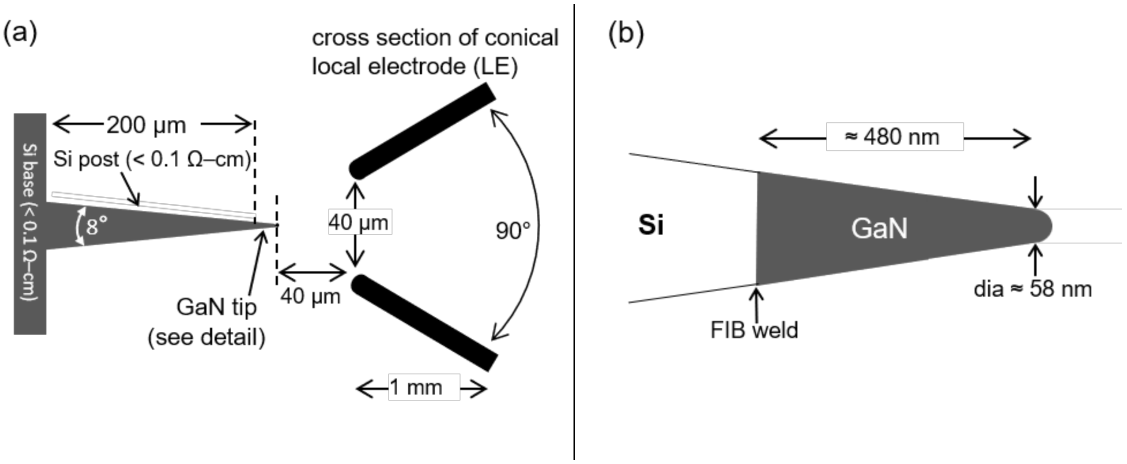

Figure 20

(a) Schematic showing tip mount and LE for electrostatic simulation of specimen used in recon 32. The Si post is given the same taper as the GaN tip. The conical LE geometry and dimensions are adapted from Ref. [44] with thickness of LE cone wall = 2 µm and radius of curvature of the wall edge facing tip = 1 µm. Tip—LE separation and post height are representative. (b) Detail showing schematic of tip used in recon 32 at the end of APT data acquisition. The residual GaN length and resulting tip diameter are indicated. For purposes of electrostatic simulations, the FIB weld is assumed to be an ohmic contact between Si and GaN.

4.1. Isotropic approximation

We assume the material has a dielectric constant of 8.9 and is isotropic. The realistic estimate for the *n*-type free carrier concentration used is 1×10^{17}cm^{-3}. The tip-electrode voltage is set to 4 kV in conformance to the approximate voltage at the end of data acquisition sessions for recon 32. A finite-element Poisson solution scheme was developed and implemented. The results show that the *n*-type specimen tip at a temperature of 54 K is fully depleted of bulk free carriers for SV ≈ 4 kV. However, an SV of 4 kV will induce an inversion layer of free holes in a region of the tip encompassing the apex. The conducting inversion layer will effectively screen the applied electric field from the interior of the specimen and the resulting on-axis, maximum surface field at the specimen apex of $E_a \sim 24$ V/nm. Moreover, the conducting inversion layer will also screen a tangential dipole field on the apex, arising from the built-in spontaneous polarization. Therefore, as described previously, a perturbation of E_a due to $\vec{P}_S$ may be ignored.

It is instructive to note that according to Mancini, et al.[7], post-ionization theory predicts that an effective surface field of ~ 24 V/nm should yield roughly stoichiometric GaN. However, Figs. 17 (b—e) illustrate that GaN stoichiometry is N rich (~ 45 at.% Ga, 55 at.% N) in the vicinity of the tip apex where the (computed) $E_a \sim 24$ V/nm, but when averaged over ROIs placed transverse to the tip axis, the composition is approximately stoichiometric. Moreover, Figs. 17 (b—e) also illustrate that the Ga^{2+}/Ga^{1+} CSR vary both radially and azimuthally (by roughly a factor of 10) with respect to the long axis of the tip. Taken together, these observations underscore the importance, as motivated in part by Mancini, et al.[7], to establish direct relationships between local values of E_s, composition, and CSR.

To conclude this section, we compare our electrostatic computation of E_a (for a semiconducting GaN specimen tip) with estimates derived from the k-factor approximation.[3] In the k-factor approach, which was originally derived for metal tips, $E_a = V_o/k\rho$ where V_o is the electrode-tip voltage, ρ is the radius of curvature of the tip, and k is a dimensionless fitting parameter with $1.5 < k < 8.5$. Background for this approximation is presented elsewhere.[24] Given the apex diameter and bias voltage for the tip under discussion (recon 32), we find that $k = 4.0$, i.e., well within the span of validity. However, it must be kept in mind that the specimen tip is an n-type semiconductor, and although it is biased to depletion under the SV, a p-type inversion layer forms on a region of the tip encompassing the apex. Therefore, the vicinity of the apex undergoing field evaporation is highly conductive and k-factor approximation can be employed. In general, however, k-factor approach for computing E_a should be used with care since it is only valid under very specialized circumstances of a highly conducting tip and will certainly not generalize to complex, multilayer specimens composed, e.g., of metals, dielectrics, and semiconductors—subjected to various SV conditions that may induce depletion and/or inversion in the vicinity of the tip apex. Further consideration of these points is given elsewhere.[24]

5. Discussion of uncertainties

There are numerous sources of uncertainty that can influence the APT-derived assessment of composition. In Sections 5.1—5.5 we describe what we regard as the more significant of these issues in their order of importance. Some representative examples for the *c*-axis specimens are illustrated using sample h; other *c*-axis samples displayed similar trends and need not be presented in similar detail.

5.1. Ambiguous assignments in the range of (14—16) Da

Although one can make various plausibility argument supporting the selection of NH_x or N_2H_x for assignment to the (14—16) Da range, the justification of choosing one over the other is still an open question. Consider for example APT analysis of just GaN. For the TLROI GaN-only section of recon 1(a), the composition is 45 at.% Ga and 55 at.% N, which is clearly off stoichiometry. On the other hand, in our prior work with APT analysis of GaN nanowires [5], running with a PE of 2 fJ and T = 54 K, and selecting N_2H_x, would return a composition of 48 at.% Ga and 52 at.% N—which is more approaching stoichiometry. Hence, assigning the (14—16) Da range becomes problematic when GaN stoichiometry is the only metric since other factors may certainly be relevant, i.e., tip shape, magnitude of E_a, and so on.

As the data herein shows, the situation for the ternary InGaN has additional complications. For example, the N fraction in the InGaN regions should ideally be 50 at.%. For T = 54 K, the only examples where this constraint is approximately met for sample h, and the In concentration is simultaneously within RBS uncertainty, are ROI 2 of recon 4 (PE = 50 fJ) and ROI 2 of recon 5 (PE = 100 fJ). However, at these PE levels, the apparent compositions in the GaN portions of the respective TLROIs is necessarily quite Ga-rich. Taken together, the general trend revealed by assigning the (14—16) Da range to NH_x is to force the N concentration to trend toward the physically-correct 50 at.% within the InGaN regions, but at the expense of the In concentration exceeding the RBS results.

5.2. Hydrogen

Hydrogen in an inescapable background contaminant in the APT tool and it can also be present both in and on a specimen tip. [1, 3] Furthermore, H may also exist as a contaminant in GaN.[45] We generally find that the measured (elemental) H concentration depends upon PE. For example, in ROI 1 of recon 1 (PE = 2 fJ) H^{1+} is observed with a fractional concentration of ≈ 0.04 at.%. In ROI 1 of recon 5 (PE = 50 fJ) H^{1+}, H_2^{1+} and H_3^{1+} are all observed and yield a fractional elemental concentration for H of ≈ 0.8 at.%. Of course, the assignment of H_2^{1+} is indistinguishable from possible He^{2+}—which is rather unlikely.

Regardless of its actual spatial origin, e.g., background, tip surface adsorbate, photo-desorbed from the chamber walls, or bulk chemical constituent of the tip, hydrogen is mobile in the strong electric field near the tip and it can readily form complex species with other constituent nitrogen species. Also, for all of the PE cases above 2 fJ, the relative counts between 14 Da and 15 Da cannot be reconciled by the isotopic ratio provided with a N^{1+} assignment; a possible alternative choice is to assign 14 Da to N_2^{2+} and 15 Da to $N_2H_2^{2+}$.

In adopting these possible alternative assignments, the net H concentrations for ROI 1 (PE = 2 fJ) of recon1 and ROI 1 of recon 4 (PE = 50 fJ) becomes ≈ 0.2 at. % and ≈ 0.8 at. %, respectively. At higher PE levels, a 16 Da peak emerges that we assign to $N_2H_4^{2+}$, but may also arise from O_2^{2+}. Therefore, even if we assume all the H originally resides within the specimen tip, inclusion of the H counts will have a negligible on the APT-derived concentration of indium. Additionally, we note that axial concentration profiles for H of the TLROIs generally show a monotonic increase with depth. Such behavior would support the argument that H is primarily a surface contaminant since the tips are conical and the surface area interrogated necessarily increases as ions are field-evaporated away. By comparison, going back and examining our separate APT analysis of uniform-diameter GaN nanowires [5], reveals that TLROI *z*-axial concentration profiles for H are correspondingly uniform along the entire ~1.6 μm length examined.

5.3. PE-dependent ambiguity for assignment of $^{113}In^{2+}$

Besides PE-dependent issues associated with N and H, the ranging of the mass-spectral peak at ≈ 56.45 Da also shows a PE-dependent ambiguity. For PE in the range of (2—50) fJ, the isotopic ratio of the In^{2+} peaks favor assigning 56.46 Da to indium. However, for PE > 50 fJ the relative counts between peaks near 55.46 Da and 56.46 Da supports an assignment to GaN_3^{2+}. Performing a Saxey-plot analysis may help elucidate these observations.[46] However, such distinctions are academic within the present context since they will have a negligible effect on the assessment of indium concentration at the relative count levels observed. Nonetheless, they are worth pointing out as sources of error that could complicate other IVAS analyses, e.g., assessment of In clustering.[47]

5.4. 2D plots of relative Ga density, spatial dependence of Ga and In CSRs, and possibility of FIB-induced Ga implantation

Figure 7 concerns sample h and indirectly reveals the 6-fold rotational symmetry about the *c*-axis expected for the wurtizite structure; it also suggests that there could be an associated 6-fold dependence of the concentration profile that originates from crystal symmetry. However, Figs. 9 (a, b) illustrate that for this relatively low PE case (2 fJ), such an azimuthal dependence of the concentration profile is insignificant. Nonetheless, the radial dependence of the concentration is seen when Ga is decomposed into its three observed charge states. Figs. 10 (a, c) show that the combined Ga^{2+} and Ga^{3+} counts dominate the center of the reconstruction while Ga^{1+} falls to a minimum at the center. This effect is consistent with a purely electrostatic artifact described earlier. Interestingly, however, for sample h with PE = 2 fJ, the radial dependence of the indium concentration and CSR does not directly mimic that of Ga; Figs. 10 (b, d) illustrate that indium concentration is dominated by combined In^{2+} and In^{3+} counts across the entire diameter of the reconstruction while In^{1+} is a minor contribution. The evolution of these effects for *c*-plane samples as the PE is increased is discussed next.

The radial concentration profiles for Ga and N (with respect to the TLROI) for sample h, where PE = 100 fJ, are illustrated in Figs. 13 (a) and 14 (a). With increasing PE, the expected trend for Ga emerges (Ref. [6]) whereby the Ga concentration profile is entirely dominated by Ga^{1+}—albeit Ga^{1+} shows a relative minimum at the center of the reconstruction. However, the situation for indium is more complicated. As shown in Figs. 13 (b) and 14 (b), the radial concentration profiles of In^{1+} and In^{2+} vary in an opposing sense such that they add up to an approximately uniform indium concertation across the diameter of the reconstruction.

Choice of the 20 nm dia ROI 2 was guided by the observation that over various PE cases for *c*-axis GaN, the axial concentration profiles for Ga and N (in the GaN portions of the recons) are closer to (physically) expected equality than for the associated TLROIs. Examples of such behavior for PE = 2 fJ, 10 fJ, and 100 fJ are shown in Figs. 6 (b), 11 (b), and 12 (b), respectively. However, this trend does not continue into the InGaN regions for all the samples. In particular, for samples h and f (higher indium concentrations) Tables 3 and 4 indicate that for a given PE up to ≈ (50—100) fJ the integrated Ga, N, and In concentrations are roughly equivalent in the corresponding ROI 1 and ROI 2. For sample c (lowest In concentration) the difference between the integrated concentrations between ROIs 1 and 2 emerges for PE ≈ 50 fJ.

The asymmetric, *c*-axis evolution of *m*-plane GaN tips was described in Section 3.1.2 and illustrated in Figs. 16—19. The apparent correlation with growth habit and PEC was also discussed. It is worth noting, however, that even though our electrostatic analysis precluded a direct influence of $\vec{P_S}$ upon E_a in defining how an *m*-plane tip would evolve as ions are field-evaporated away, we point out that Megalini[42] attributed the polarity-dependent asymmetry in *c*-axis PEC etching to a mechanism whereby photo-generated holes drift under the action of $\vec{P}_S$. Thus, insofar as laser-assisted field evaporation is somewhat analogous to a PEC etch process in defining the evolution of a biased semiconductor APT tip, e.g., photoelectrons pulled to the tip base, photogenerated holes pulled to the tip apex, and the generation and emission of positive ions, the role of spontaneous polarization deserves further study in efforts to identify the precise physical mechanism responsible for the observed asymmetric tip evolution.

Concerns have also been raised regarding compositional errors that could arise from unintentional FIB-induced implantation of Ga ions during tip preparation.[48] However, we find no significant difference in the PE-dependent composition for single GaN nanowires [5], which did not require any FIB milling, with trends revealed in the present study. The issue of FIB induced Ga implantation is of lesser concern for analyses within ROIs that omit sections that encompass the implantation depth, or experimental situations where the tip surface is outside of the field-of-view on the detector. Finally, the use of Ne FIB for APT specimen preparation may provide a means to avoid such possible Ga contamination altogether.[49]

5.5. Dependence of ion counts on ROI placement and depth

Another source of uncertainty is that the detected ion counts within an ROI can depend upon its orientation and placement. Figure 21 (a) illustrates the placement of 3 ROI cylinders that are oriented axially in the TLROI of recon 32. The associated graphs, Figs. 21 (b, c, d), show the depth dependence of the ion counts for Ga, N, and In. The placement of these ROIs is chosen to roughly conform to a similar analysis of *m*-plane GaN as described in Ref. [22]. For each case, the total detected counts near the tip apex is greater than the counts for the maximum depth indicated. The effect is most pronounced for ROI 2 of Fig. 21 (b). Also, while both ROI 1 and 2 fall on the “laser facing” side of the TLROI, the total counts associated with ROI 2 are substantially higher.

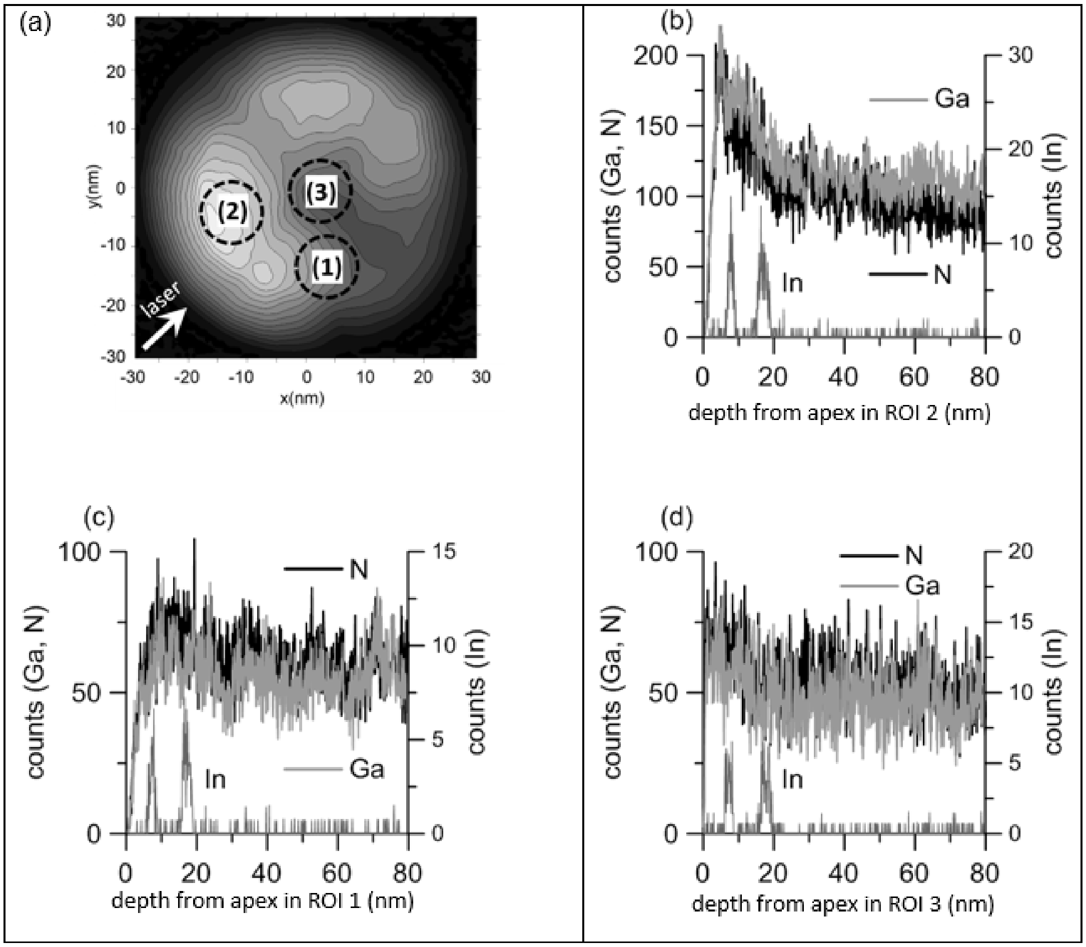

Figure 21

Spatial dependence of detected counts in *m*-plane sample of recon 32 with PE = 20 fJ. (a) The 2D map of Fig. 16 is used to place ROI cylinders labeled 1—3, each of 10 nm diameter, and oriented parallel to the *m* axis. The placement and diameter of the ROIs is chosen to approximately conform with similar work described in Ref. [22]. (b) Axial dependence of detected counts of Ga, N, and In for ROI 2, (c) ROI 1, and (d) ROI 3. Note the changes in the vertical scales for the three cases. The intersection of the curved tip of the TLROI with ROI cylinders 2 and 1 results in the abrupt rise in Ga and N counts shown in (b) and (c). The artifact is not seen in (d) since ROI 3 is placed at the tip apex.

The spatial dependence of ion counts for a *c*-plane specimen (recon 3) is shown in Fig. 22. Here again, the ROI on the “laser facing” side shows the greater overall counts, however, the ROI on the “laser shadowed” side shows very similar depth-dependent behavior. The coaxially-placed ROI shows the lowest, but most uniform, counts as a function of depth.

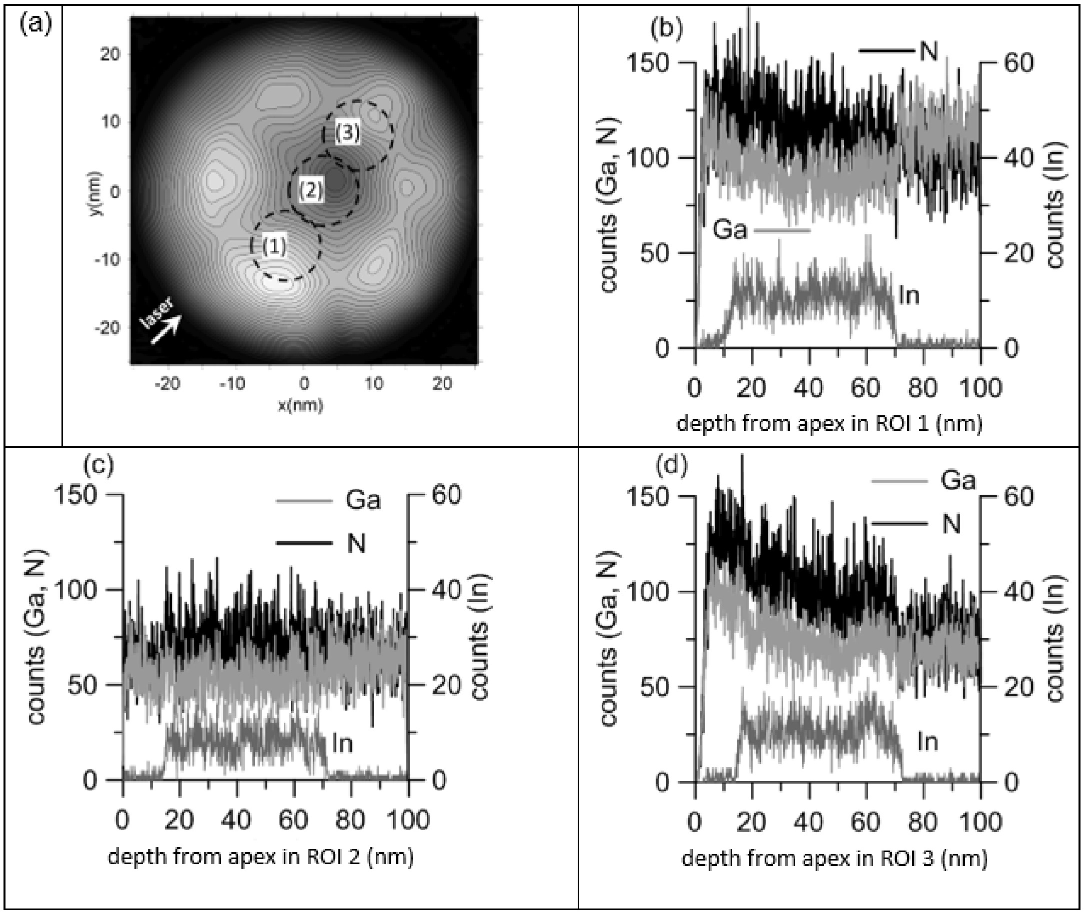

Figure 22

Spatial dependence of detected counts in *c*-plane sample of recon 3 with PE = 10 fJ. (a) 2D relative density map for Ga (similar to that of Fig. 7) is used to place ROI cylinders labeled 1—3, each of 10 nm diameter, and oriented parallel to the z axis. The grayscale is omitted for brevity. (b) Axial dependence of detected counts of Ga, N, and In for ROI 1, (c) ROI 2, and (d) ROI 3. Note the changes in the vertical scales for the three cases. The intersection of the curved tip of the TLROI with ROI cylinders 1 and 3 results in the abrupt rise in Ga and N counts shown in (b) and (d). The artifact is not seen in (c) since ROI 2 is placed at the tip apex. For all cases in (b—d), the bin width per depth increment is 0.1 nm.

The physical origin of these effects is not immediately clear, and we hesitate to speculate on their nature but opt instead to simply report the observations. However, mechanisms proposed by Riley, et al.[22] may apply. Whatever their origin, these results show that the assessment of uncertainty can be a rather complex issue. For example, while concentration profiles within an ROI may indicate a spatially dependent composition ratio, the absolute number of counts may also be spatially dependent.

5.6. Comments on reconstruction fitting parameters

In generating reconstructions, one is generally compelled to regard DE, ICF, and S/C as fitting parameters, rather than physical quantities. These parameters are often chosen from experience and intuition to force the reconstruction to conform with separately measured features of the specimen tip. Such measured features can include length of material removed in APT, thickness of layers, and so on. Moreover, in varying these parameters one can often generate reconstructions that conform to measured dimensions even if the volume-per-ion, which is input into the IVAS software, is incorrect. Indeed, the software offers default options to automatically choose ion volumetric data regardless of the actual material under consideration. Therefore, in the absence of correlative imaging methods (TEM, FESEM, etc.) to help refine recon parameters, solely using APT reconstruction methods to infer reliable structural, crystallographic, and density information should be approached with caution.

6. Conclusions

APT was performed on a series of four, *c*-plane GaN/$In_xGa_{1-x}N$/GaN test structures with $x = 0.112$, 0.056, 0.034 and 0.030 as separately determined by RBS. The estimated RBS uncertainty for In concentration was ± 0.5 at.%. The base temperature for most APT measurements was 54 K but also included various cases run at 26 K. For the respective values of mole fraction x indicated, APT returned In concentrations within RBS uncertainty for laser pulse energies in the ranges of (2—50) fJ, (2—10) fJ, (2—100) fJ, and (2—50) fJ. Assigning the mass-spectral range within (14—16) Da to ionic complexes of NH_x or N_2H_x did not significantly change the measurements of In concentrations, nor did parsing the APT data into single-hit detector events or multiple-hit detector events.

APT was also performed on *m*-plane specimen tips prepared from *c*-axis grown, GaN/InGaN/GaN core-shell, quantum well nanorod structures. Concentration profiles for Ga^{2+} and Ga^{1+} (in the GaN core region) viewed along [0001] revealed a spatial asymmetry that correlated with a displacement of the tip apex in the $[000\bar{1}]$ direction as ions are field-evaporated away. When viewed along $[\bar{1}2\bar{1}0]$, both the tip apex and concentration profiles for Ga^{2+} and Ga^{1+} were essentially symmetric. The symmetry of the APT tip evolution was found to correlate with both the growth habit of *m*-axis GaN nanostructures, and the anisotropic photo-electrochemical etching of *m*-plane GaN. Additionally, the APT measured indium concentration in the quantum wells was in approximate agreement with estimates derived from photoluminescence.

Electrostatic simulations were performed on realistic cases of *n*-type GaN tip-electrode geometry and tip-electrode bias. The results revealed that the formation of a conducting, *p*-type inversion layer over the tip apex would preclude the possibility that the apex surface field could be perturbed by the strong built-in spontaneous polarization (known to exist in GaN), since the polarization-induced surface charge would be screened by the free holes in the inversion layer. Our simulations also reveal that in APT analysis of semiconductors, for cases where a conducting inversion layer is present, the apex surface field may be estimated using the simplified *k*-factor approximation, which was originally derived for metal tips. However, if the tip is variously composed of insulating, conducting, and semiconducting portions, the *k*-factor approximation will likely be invalid.

Reconstruction analysis of both *c*-plane and *m*-plane specimens revealed variations in detected counts, which depended upon ROI placement and analysis depth. This effect may produce spatially dependent variations in the fractional uncertainties of the detected species. Therefore, these issues should be considered when estimating spatially dependent uncertainties in APT results.

7. Acknowledgments

The authors gratefully acknowledge insightful discussions with A. N. Chiaramonti, K. A. Bertness, D. R. Diercks, and B. L. Gorman. Valuable and constructive commentary from the reviewers is also acknowledged.

The National Institute of Standards and Technology (NIST) supported the contributions of NIST-affiliated authors.

Authors affiliated with the University of New Mexico acknowledge that the nanostructure growth work was supported by the Defense Advanced Research Projects Agency (DARPA) under award number D13AP00055 and by the NSF under cooperative agreement EEC-0812056. Any opinions, findings, and conclusions or recommendations expressed in this material are those of the author(s) and do not necessarily reflect the views of DARPA or the National Science Foundation.

8. References

[1] Gault B, Moody MP, Cairney JM (2012) *Atom Probe Microscopy* (Springer, New York).

[2] Larson D, Valley J, Ushikubo T, Miller M, Takamizawa H, Shimizu Y, Gordon LM, Joester D, Giddings D, Reinhard DA, Prosa TJ, Olson DP, Lawrence DF, Clifton PH, Ulfig RM, Martin I, Kelly TF (2013) New Applications in Atom Probe Tomography. *Microscopy and Microanalysis* 19:1022-1023. https://doi.org/10.1017/S1431927613007101

[3] Larson DJ, Prosa TJ, Ulfig RM, Geiser BP, Kelly TF (2013) *Local Electrode Atom Probe Tomography* (Springer, New York An approximate method to calculate the surface field on a biased tip is given on page 62; formality supporting this scheme for a strictly conducting tip is given by P. J. Birdseye and D. A. Smith, Surf. Sci. 23, 198 (1970).).

[4] Miller MK (2000) *Atom Probe Tomography, Analysis at the Atomic Level* (Kluwer Academic, New York).

[5] Sanford NA, Blanchard PT, Brubaker M, Bertness KA, Roshko A, Schlager JB, Kirchhofer R, Diercks DR, Gorman B (2014) Laser-assisted atom probe tomography of MBE grown GaN nanowire heterostructures. *Physica Status Solidi C: Current Topics in Solid State Physics, Vol 11, No 3-4,* Physica Status Solidi C-Current Topics in Solid State Physics, eds Eddy CR, Kuball M, Koleske DD, & Amano H), Vol. 11, pp 608-612.

[6] Rigutti L, Bonef B, Speck J, Tang F, Oliver RA (2018) Atom probe tomography of nitride semiconductors. *Scripta Materialia* 148:75-81. https://doi.org/10.1016/j.scriptamat.2016.12.034

[7] Mancini L, Amirifar N, Shinde D, Blum I, Gilbert M, Vella A, Vurpillot F, Lefebvre W, Larde R, Talbot E, Pareige P, Portier X, Ziani A, Davesnne C, Durand C, Eymery J, Butte R, Carlin J-F, Grandjean N, Rigutti L (2014) Composition of Wide Bandgap Semiconductor Materials and Nanostructures Measured by Atom Probe Tomography and Its Dependence on the Surface Electric Field. *Journal of Physical Chemistry C* 118(41):24136-24151. https://doi.org/10.1021/jp5071264

[8] DiRusso E, Blum I, Houard J, Gilbert M, Costa Gd, Blavette D, Rigutti L (2018) Compositional accuracy of atom probe tomography measurements in GaN: Impact of experimental parameters and multiple evaporation events. *Ultramicroscopy* 187:126-134. https://doi.org/ff10.1016/j.ultramic.2018.02.001

[9] Diercks DR, Gorman BP, Kirchhofer R, Sanford N, Bertness K, Brubaker M (2013) Atom probe tomography evaporation behavior of C-axis GaN nanowires: Crystallographic, stoichiometric, and detection efficiency aspects. *Journal of Applied Physics* 114(18):184903. https://doi.org/10.1063/1.4830023

[10] Okamoto H (2006) Supplemental literature review. *Journal of Phase Equilibria and Diffusion* 27(5):535-535. https://doi.org/10.1007/bf02736467

[11] Agrawal R, Bernal RA, Isheim D, Espinosa HD (2011) Characterizing Atomic Composition and Dopant Distribution in Wide Band Gap Semiconductor Nanowires Using Laser-Assisted Atom Probe Tomography. *Journal of Physical Chemistry C* 115(36):17688-17694. https://doi.org/10.1021/jp2047823

[12] Hono K, Ohkubo T, Chen YM, Kodzuka M, Oh-ishi K, Sepehri-Amin H, Li F, Kinno T, Tomiya S, Kanitani Y (2011) Broadening the applications of the atom probe technique by ultraviolet femtosecond laser. *Ultramicroscopy* 111(6):576-583. https://doi.org/10.1016/j.ultramic.2010.11.020

[13] Prosa T, Lenz D, Martin I, Reinhard D, Larson D, Bunton J (2021) Evaporation-Field Differences with Deep-UV Atom Probe Tomography. *Microsc Microanal* 27:1262-1264. https://doi.org/10.1017/S1431927621004736

[14] Devaraj A, Colby R, Hess WP, Perea DE, Thevuthasan S (2013) Role of Photoexcitation and Field Ionization in the Measurement of Accurate Oxide Stoichiometry by Laser-Assisted Atom Probe Tomography. *Journal of Physical Chemistry Letters* 4(6):993-998. https://doi.org/10.1021/jz400015h

[15] Diercks DR , Gorman BP (2015) Nanoscale Measurement of Laser-Induced Temperature Rise and Field Evaporation Effects in CdTe and GaN. *Journal of Physical Chemistry C* 119(35):20623-20631. https://doi.org/10.1021/acs.jpcc.5b02126

[16] Muth JF, Lee JH, Shmagin IK, Kolbas RM, Casey HC, Keller BP, Mishra UK, DenBaars SP (1997) Absorption coefficient, energy gap, exciton binding energy, and recombination lifetime of GaN obtained from transmission measurements. *Applied Physics Letters* 71(18):2572-2574. https://doi.org/10.1063/1.120191

[17] Robins LH, Armstrong JT, Marinenko RB, Vaudin MD, Bouldin CE, Woicik JC, Paul AJ, Thurber WR, Miyano KE, Parker CA, Roberts JC, Bedair SM, Piner EL, Reed MJ, El-Masry NA, Donovan SM, Pearton SJ (2000) Optical and structural studies of compositional inhomogeneity in strain-relaxed indium gallium nitride films. *2001 IEEE International Symposium on Compound Semiconductors*:507-512. https://doi.org/10.1109/iscs.2000.947207

[18] Sanford NA, Chiaramonti Debay A, Gorman BP, Diercks DR (2018) Hybrid extreme ultraviolet imaging spectrometer. United States Patent 9 899 197.

[19] Sanford NA , Chiaramonti Debay A (2018) Imaging spectrometer. United States Patent 10 153 144.

[20] Chiaramonti AN, Miaja-Avila L, Caplins BW, Blanchard PT, Diercks DR, Gorman BP, Sanford NA (2020) Field Ion Emission in an Atom Probe Microscope Triggered by Femtosecond-Pulsed Coherent Extreme Ultraviolet Light. *Microscopy and Microanalysis* 26(2):258-266. https://doi.org/10.1017/s1431927620000203

[21] Miaja-Avila L, Caplins BW, Chiaramonti AN, Blanchard PT, Brubaker MD, Davydov AV, Diercks DR, Gorman BP, Rishinaramangalam A, Feezell DF, Bertness KA, Sanford NA (2021) Extreme Ultraviolet Radiation Pulsed Atom Probe Tomography of III-Nitride Semiconductor Materials. *Journal of Physical Chemistry C* 125(4):2626-2635. https://doi.org/10.1021/acs.jpcc.0c08753

[22] Riley JR, Detchprohm T, Wetzel C, Lauhon LJ (2014) On the reliable analysis of indium mole fraction within InxGa1-xN quantum wells using atom probe tomography. *Applied Physics Letters* 104(15):152102. https://doi.org/10.1063/1.4871510

[23] Riley JR, Bernal RA, Li Q, Espinosa HD, Wang GT, Lauhon LJ (2012) Atom Probe Tomography of a-Axis GaN Nanowires: Analysis of Nonstoichiometric Evaporation Behavior. *Acs Nano* 6(5):3898-3906. https://doi.org/10.1021/nn2050517

[24] Zhang Q, Klein B, Sanford NA, Chiaramonti Debay AN (2021) Comparative Apex Electrostatics of Atom Probe Tomography Specimens. *Journal of Electronic Materials* 50:3022-3029. https://doi.org/10.1007/s11664-021-08932-6

[25] Sanford NA, Munkholm A, Krames MR, Shapiro A, Levin I, Davydov AV, Sayan S, Wielunski LS, Madey TE (2005) Refractive index and birefringence of InxGa1-xN films grown by MOCVD. *Physica Status Solidi C - Conferences and Critical Reviews, Vol 2, No 7,* Physica Status Solidi C-Current Topics in Solid State Physics, ed Stutzmann M), Vol. 2, pp 2783-2786.

[26] Sanford NA, Blanchard PT, White R, Vissers MR, Diercks DR, Davydov AV, Pappas DP (2017) Laser-assisted atom probe tomography of Ti/TiN films deposited on Si. *Micron* 94:53-65. https://doi.org/10.1016/j.micron.2016.12.001

[27] Thompson K, Lawrence D, Larson DJ, Olson JD, Kelly TF, Gorman B (2007) In situ site-specific specimen preparation for atom probe tomography. *Ultramicroscopy* 107(2-3):131-139. https://doi.org/10.1016/j.ultramic.2006.06.008

[28] Hersee SD, Sun X, Wang X (2006) The controlled growth of GaN nanowires. *Nano Letters* 6(8):1808-1811. https://doi.org/10.1021/nl060553t

[29] Nami M, Eller RF, Okur S, Rishinaramangalam AK, Liu S, Brener I, Feezell DF (2017) Tailoring the morphology and luminescence of GaN/InGaN core-shell nanowires using bottom-up selective-area epitaxy. *Nanotechnology* 28(2):025202. https://doi.org/10.1088/0957-4484/28/2/025202

[30] Rishinaramangalam AK, Ul Masabih SM, Fairchild MN, Wright JB, Shima DM, Balakrishnan G, Brener I, Brueck SRJ, Feezell DF (2015) Controlled Growth of Ordered III-Nitride Core-Shell Nanostructure Arrays for Visible Optoelectronic Devices. *Journal of Electronic Materials* 44(5):1255-1262. https://doi.org/10.1007/s11664-014-3456-z

[31] Miller MK , Forbes RG (2014) *Atom-Probe Tomography: The Local Electrode Atom Probe* (Springer Science+Business Media, New York).

[32] Anonymous (*International Centre for Diffraction Data, Powder Diffraction File*. Available at http://www.icdd.com.

[33] O'Donnell KP, Mosselmans JFW, Martin RW, Pereira S, White ME (2001) Structural analysis of InGaN epilayers. *Journal of Physics-Condensed Matter* 13(32):6977-6991. https://doi.org/10.1088/0953-8984/13/32/307

[34] Kingham DR (1982) The post-ionization of field evaporated ions - a theoretical explanation of multiple charge states. *Surface Science* 116(2):273-301. https://doi.org/10.1016/0039-6028(82)90434-4

[35] Cullity BD (1967) *Elements of X-Ray Diffraction* (Addision-Wesley, Reading, MA).

[36] Haus HA , Melcher JR (1989) *Electromagnetic Fields and Energy* (Prentice Hall, Englewood Cliffs, NJ).

[37] Reitz JR , Milford FJ (1967) *Foundations of Electromagnetic Theory* (Addision-Wesley, Reading, MA).

[38] Pal J, Tse G, Haxha V, Migliorato MA, Tomic S (2012) Importance of non linear piezoelectric effect in Wurtzite III-N semiconductors. *Optical and Quantum Electronics* 44(3-5):195-203. https://doi.org/10.1007/s11082-011-9518-z

[39] Bernardini F, Fiorentini V, Vanderbilt D (1997) Spontaneous polarization and piezoelectric constants of III-V nitrides. *Physical Review B* 56(16):10024-10027. https://doi.org/10.1103/PhysRevB.56.R10024

[40] Stutzmann M, Ambacher O, Eickhoff M, Karrer U, Pimenta AL, Neuberger R, Schalwig J, Dimitrov R, Schuck PJ, Grober RD (2001) Playing with polarity. *Physica Status Solidi B-Basic Research* 228(2):505-512. https://doi.org/10.1002/1521-3951(200111)228:2<505::Aid-pssb505>3.3.Co;2-l

[41] Jindal V , Shahedipour-Sandvik F (2009) Theoretical prediction of GaN nanostructure equilibrium and nonequilibrium shapes. *Journal of Applied Physics* 106(8):083115. https://doi.org/10.1063/1.3253575

[42] Megalini L (2013) Current Aperture III-Nitride Edge-Emitting Blue Laser Diode, Master of Science Thesis,Department of Electrical Engineering, University of California, Santa Barbara, CA. ( ). Available at

[43] Li H, Geelhaar L, Riechert H, Draxl C (2015) Computing Equilibrium Shapes of Wurtzite Crystals: The Example of GaN. *Physical Review Letters* 115(8):085503. https://doi.org/10.1103/PhysRevLett.115.085503

[44] Bajikar SS, Kelly TF, Camus PP (1996) Electrostatic analysis of local-electrode atom probes. *Applied Surface Science* 94-5:464-471. https://doi.org/10.1016/0169-4332(95)00411-4

[45] Nickel NH ed (1999) *Hydrogen in Semiconductors II (Semiconductors and Semimetals)* (Academic Press, New York), Vol. 61.

[46] Saxey DW (2011) Correlated ion analysis and the interpretation of atom probe mass spectra. *Ultramicroscopy* 111(6):473-479. https://doi.org/10.1016/j.ultramic.2010.11.021

[47] Moody MP, Stephenson LT, Ceguerra AV, Ringer SP (2008) Quantitative binomial distribution analyses of nanoscale like-solute atom clustering and segregation in atom probe tomography data. *Microscopy Research and Technique* 71(7):542-550. https://doi.org/10.1002/jemt.20582

[48] Tang F, Moody MP, Martin TL, Bagot PAJ, Kappers MJ, Oliver RA (2015) Practical Issues for Atom Probe Tomography Analysis of III-Nitride Semiconductor Materials. *Microscopy and Microanalysis* 21(3):544-556. https://doi.org/10.1017/s1431927615000422

[49] Allen F, Notte J, Xia D, Blanchard PT, Zhang R, Minor A, Sanford N (2020) Neon-FIB for the Fabrication of Tips for Atom Probe Tomography and Electgron Tomography. *Microscopy and Microanalysis* 26:184. https://doi.org/https://doi.org/10.1017/S1431927620013719